

# Poro-Serrated trailing edge devices for airfoil self-noise reduction

Alexandros Vathylakis<sup>1</sup> and Tze Pei Chong<sup>2</sup>  
*Brunel University London, Uxbridge, England UB8 3PH, United Kingdom*

and

Phillip F. Joseph<sup>3</sup>  
*ISVR, University of Southampton, Southampton, England SO17 1BJ, United Kingdom*

**This paper represents the continuation of the works previously published in Chong et al. (“Self-Noise Produced by an Airfoil with Nonflat Plate Trailing-Edge Serrations,” *AIAA Journal*, Vol. 51, No. 11, 2013, pp. 2665–2677), who used several nonflat plate serrated trailing edges for the reduction of airfoil self-noise. The poro-serrated concept developed in the current work improves substantially the overall noise performance of the nonflat plate trailing-edge serration type. The use of porous metal, synthetic foams, or thin brush bundles to fill the gaps between adjacent members of the sawtooth can completely suppress the bluntness-induced vortex shedding tonal noise. Most important, up to 7 dB turbulent boundary layer–trailing-edge broadband noise reduction can simultaneously be achieved without compromising the aerodynamic performances in lift and drag. The poro-serrated trailing edges do not cause any noise increase throughout the frequency range investigated here. The reduction of the turbulent broadband noise is primarily caused by the serration effect, but under a condition that the sawtooth surface must be solid and nonporous. The primary role of the porous metal foams in a poro-serrated trailing edge is to suppress the vortex shedding tonal noise. However, an optimum selection of the porous material is also found to be able to further reduce the broadband noise level. The new serrated trailing-edge concept developed here has the potential to improve the industrial worthiness of the serration technology in achieving low noise radiation in fan and turbine blades.**

---

<sup>1</sup>Research Assistant, College of Engineering, Design and Physical Sciences; [alex.vat@hotmail.com](mailto:alex.vat@hotmail.com). Non-AIAA member.

<sup>2</sup>(CORRESPONDING AUTHOR) Senior Lecturer, College of Engineering, Design and Physical Sciences; [t.p.chong@brunel.ac.uk](mailto:t.p.chong@brunel.ac.uk). Member AIAA

<sup>3</sup>Professor, Institute of Sound and Vibration Research; [pfj@isvr.soton.ac.uk](mailto:pfj@isvr.soton.ac.uk). Member AIAA.

## Nomenclature

$2h$	=	<i>serration length (root-to-tip distance), mm</i>
$C$	=	<i>airfoil chord length, m</i>
$f$	=	<i>frequency, Hz</i>
$U$	=	<i>mean flow velocity, <math>ms^{-1}</math></i>
$x$	=	<i>streamwise direction measuring from the airfoil leading edge, mm</i>
$y$	=	<i>wall-normal direction, mm</i>
$z$	=	<i>spanwise direction, mm</i>
$\alpha$	=	<i>angle of attack for the airfoil, deg</i>
$\Delta\xi$	=	<i>difference in <math>\xi</math> measured by the surface-mounted hot-film sensor between a straight and a poro-serrated trailing edge, dB</i>
$\Delta SPL$	=	<i>difference in sound pressure level between a baseline (straight) and a treated trailing edge, dB</i>
$\varepsilon$	=	<i>bluntness of saw tooth trailing edge at the root region, mm</i>
$\lambda$	=	<i>serration period, mm</i>
$\Theta$	=	<i>polar angles of the microphone relative to the jet flow centerline, deg</i>
$\xi$	=	<i>power spectral density measured by surface-mounted hot-film sensor, dB</i>
$\phi$	=	<i>mean square fluctuating velocity, <math>(ms^{-1})^2/Hz</math></i>
$\Phi$	=	<i>overall wake power spectral density of the streamwise velocity, dB</i>
$\varphi$	=	<i>serration angle, deg</i>

## I. Introduction

**I**N the middle of the last century, jet engine noise was considered to be the major source of aircraft noise. Since then, the introduction of high bypass ratio turbofan engines has meant that jet noise is now considerably reduced. Jet noise is now just one of numerous other comparable noise sources, all of which must be tackled in order to reduce the overall aero engine noise. Important noise sources on modern aeroplane are generated at the trailing edge of fan blades or the airframe's high lift devices. The noise mechanism here is by the scattering of the hydrodynamic

pressure fluctuations near the trailing edge. At high Reynolds numbers, the boundary layer develops over the airfoil surface is primarily turbulent and hence the radiated noise from the trailing edge is largely broadband in nature.

There has been much interest recently in developing methods aimed at reducing trailing edge broadband noise, such as serrated edges [1-3], porous surfaces [4] and brushes [5-6]. These passive methods have been demonstrated experimentally in low speed rig tests to afford levels of radiated noise reduction of roughly between 2 dB and 6 dB. Serrated trailing edges, in particular, have been shown to highly effective in reducing noise. In nearly all cases, however, the serrations have been formed from flat plates, which are then inserted into the trailing edge of the main airfoil body. This was done for ease of manufacture and, more importantly, to prevent vortex shedding arising from bluntness caused by cutting the serrations into the airfoil main body. Serrated flat plate inserts are unlikely to have the structural integrity for continuously operation at high loading. Moreover, introducing flat plate inserts alter the airfoil geometry and hence the global circulation around the airfoil is likely to degrade its aerodynamic performance of the original airfoil.

More preferable from the point of view of structural integrity is to cut the serration patterns directly into the airfoil body. However, whilst this configuration has also been shown to afford good level of broadband noise reduction [7], the overall noise reduction is compromised by high level of bluntness-induced narrowband vortex shedding noise. It is also envisaged that the airfoil's pressure drag will increase due to the vortex shedding in the wake. Previous attempt at reducing the bluntness-induced vortex shedding by wrapping woven-wire mesh screen around the nonflat plate serrated trailing edge was only partially successful [8]. The reason might be due to the low flow resistance of the mesh screen to be effective in suppressing the vortex shedding. Moreover, noise level is found to increase at high frequency due to the surface roughness introduced by the mesh screen to the sawtooth surface. As a result, the overall noise performance is not improved much.

A new approach to introducing serrations directly into the main body of airfoil is investigated in this paper which will be shown to achieve good levels of broadband noise reduction whilst completely suppressing vortex shedding noise at the blunt part of the serration. Central to the noise reduction strategy is the use of porous foams located between adjacent members of sawtooth to fill the gap. Note that these porous foams were cut precisely to match the exact shape of the interstices (sawtooth gaps), so that an original NACA0012 profile throughout the chord length is preserved. The flow resistance associated with the porous foam arising from loss within the foam will be shown to inhibit vortex shedding provided that the flow resistance is within some optimal range of values. If the flow

resistance of the porous foam is too high, scattering at the edge of the serration is modified to the extent that the benefits of the serrations are diminished. In this work, the investigation is mostly focused on the use of porous metal foam – nickel-chromium foam of moderate flow resistivity which has been found to almost completely suppress vortex shedding while maintaining the benefits of the serrated trailing edge. At the same time, broadband noise reduction can simultaneously be achieved without significant loss of efficiency. The combination of porous material and serration at the trailing edge, which in this paper is termed as *Poro-Serrated*, now provides two possible noise reduction mechanisms. One associated with the oblique edges due to the serrations, and the other arising from porosity which allows the pressure and suction sides to ‘communicate’, therefore reducing the acoustic dipole strength at the trailing edge. Which of these is the dominant noise reduction mechanism will be discussed later in this paper.

## II. Experimental Setup

### A. Test Model and the Trailing Edge Serrations

Similar to the previous work by the authors in [7, 8], the airfoil under investigation is a NACA0012 airfoil with a sawtooth serration cut directly into the main body of the airfoil. The chord length ( $C$ ) of the airfoil is 150 mm, and the width is 450 mm. Between the leading edge  $x/C = 0$ , and  $x/C = 0.79$ , the original NACA0012 airfoil profile is unmodified, where  $x$  is the streamwise direction. Further downstream,  $0.79 < x/C < 1.0$ , is a section that can be removed and replaced by a serration profile. Once attached the serrations form a continuous profile giving the appearance that the serrations are cut into the main body of the NACA0012 airfoil. Figure 1 shows the parameters associated with serrated trailing edge geometry. A prominent feature of this type of serrated trailing edge is the exposure of a significant bluntness ( $\varepsilon$ ) at the root region, which would otherwise be negligible for the conventional flat plate type serrated trailing edge.

A total of ten trailing edge sections, including one with straight trailing edge to serve as the baseline case, were investigated in this study. Table 1 summarizes the geometrical parameters and drawings of these trailing edge sections. In particular, the poro-serrated trailing edges  $S1^+$ ,  $S3^+$ ,  $S3^{++}$  and  $S3^{\Delta}$  represent the core of investigation in this paper. Note that between the ( $S1$ ,  $S1^+$ ) group and ( $S3$ ,  $S3^+$ ,  $S3^{++}$ ,  $S3^-$ ,  $S3^{\Delta}$  and  $S3^{\circ}$ ) group, they share the same

$2h$  and  $\varepsilon$  values but with different values of  $\varphi$  and  $\lambda/h$  (see Table 1). The S1–group of serrations therefore has a narrower sawtooth angle compared to the S3–group of serrations.

In this paper, the investigation of the poro-serrated trailing edge mainly focuses on the use of porous nickel-chromium foam at the interstices. The porous nickel-chromium foam has the following characteristics: 17–23 pores/inch, pore diameter  $\sim 0.9$  mm, and air flow resistivity  $\sim 8$  kPa s/m<sup>2</sup> (taken from data sheet). In addition, brushes and Melamine foam were also attempted at the interstices (S3<sup>Δ</sup> and S3<sup>++</sup>, respectively) to explore whether the aeroacoustic performance of the poro-serrated trailing edge could be further enhanced by different porous materials. The Melamine foam has good sound absorption property with  $\sim 180$  pores/inch and air flow resistivity  $\sim 10$  kPa s/m<sup>2</sup> (taken from data sheet). The “inversed” poro-serrated trailing edges of S3<sup>-</sup>, and other trailing edge designs S3<sup>o</sup> and SP, also utilize porous nickel-chromium foams. Further details can be found in Table 1.

As already mentioned, the porous metal forms or Melamine were cut precisely to match the exact shape of the interstices, so that the airfoil with the S1<sup>+</sup>, S3<sup>+</sup> or S3<sup>++</sup> poro-serrated trailing edge would have a continuous NACA0012 profile throughout the chord length. As an example, photograph showing the S3<sup>+</sup> poro-serrated trailing edge is shown in Fig. 2. A similar principle in maintaining the original NACA0012 profile also applies to the S3<sup>-</sup>, S3<sup>o</sup> and SP trailing edges. Tripping tapes were placed at about  $0.2C$  from the leading edge of the NACA0012 airfoil on both sides to artificially trigger the boundary layers into turbulent.

## **B. Wind Tunnel Facilities and Instrumentations**

Free field measurements of the airfoil self noise were mainly conducted in the newly commissioned open jet wind tunnel at Brunel University London, which is situated in a 4 m x 5 m x 3.4 m anechoic chamber. As shown in Fig. 3a, the nozzle exit is rectangular with dimensions of 0.10 m (height) x 0.30 m (width). This wind tunnel can achieve a turbulence intensity of between 0.1–0.2% and a maximum jet velocity of about 80 ms<sup>-1</sup>. The background noise of the wind tunnel facility is well below the self noise of the quietest airfoil across the whole range of velocity [9]. The range of jet speeds under investigation was between 20 ms<sup>-1</sup> and 60 ms<sup>-1</sup>, corresponding to Reynolds numbers based on  $C$  of  $2 \times 10^5$  and  $6 \times 10^5$  respectively. The airfoil was held by side plates and attached flushed to the nozzle lips. In this study the airfoil is kept at 0° angle of attack. Repeatability test on the S3 and S3<sup>+</sup> serrations on noise performance was made in the open jet wind tunnel at the Institute of Sound and Vibration Research (ISVR), University of Southampton [10].

As shown in Fig. 3a, far field noise measurements at the Brunel aeroacoustic wind tunnel were made by a single condenser microphone at polar angles of  $\theta = 90^\circ$  at a distance of 1.0 m from the airfoil trailing edge at mid span. Noise data was acquired at a sampling frequency of 44 kHz for 10 seconds by a 16-bit Analogue-Digital card from National Instrument. The data was then windowed and the Power Spectral Density (*PSD*) of 1 Hz bandwidth computed from a 1024 point FFT.

Also shown in Fig. 3a is an acoustic camera manufactured by GFAI Tech GmbH with a 0.35 m-diameter carbon-body planar ring array consisting of 32 microphones to beamform the noise source radiated from the airfoil. The microphones are electrets type of ¼-inches diameter (Sennheiser model 4211). The frequency response of the microphones is 20 Hz–20 kHz ( $\pm 3$ dB) with a dynamic range of 28–130 dBA. An integrated fixed focus camera is placed in the middle of the round array. The acoustic mapping data is acquired through a 24-bit data recorder with a sampling rate up to 192 kHz per analog channel. As illustrated in Fig. 3a, the array was placed on a tripod where its centre pointed upwards, focusing on the trailing edge of the airfoil at a distance of 0.67 m and a polar angle  $\theta = -90^\circ$ . The noise data was sampled at 48 kHz for 32 seconds, which was then windowed (Hamming) to estimate the *PSD* of 1 Hz bandwidth using 1024 point FFT.

Note that all the noise results presented in this paper are obtained from the single far field microphone, except the acoustic maps in Fig. 9 which are measured by the phase array microphones (beamformer).

To investigate the footprints of the vortex shedding in the wake subjected to the poro-serrated trailing edge, single hot-wire probe (5  $\mu$ m diameter, 1.25 mm length, DANTEC 55P11) was used to measure the mean and fluctuating velocities of the airfoil wake at an overheat ratio of 1.8. Signals from the hot-wire probe were digitized by a 12-bit analog-digital converter (TSI model ADCPCI) at a sampling frequency of 20 kHz for 120000 realizations. The hot-wire probe was attached to a computer-controlled two-dimensional traverse system with a resolution of 0.01 mm in both directions. To investigate the near wall turbulence near the trailing edge, a pair of glue-on hot-film sensors (0.1 mm diameter, 0.9 mm length, DANTEC 55R47) are used. The hot-film sensors were operated in a constant-temperature mode with a relatively mild overheat ratio of 1.4 to avoid adding excessive heating to the near wall boundary layer. The hot-film sensors were sampled simultaneously at 20 kHz for 120000 realizations.

Aerodynamic force measurements were made in a conventional closed working section wind tunnel at Brunel University London. This wind tunnel is not acoustically treated and is not suitable for noise measurement. Instead, it

is only used for measurements of the lift and drag forces produced by the NACA0012 airfoil with poro-serrated trailing edges. The wind tunnel has a test section of 0.5 m x 0.5 m, a maximum velocity in the test section of about 38 ms<sup>-1</sup> and a freestream turbulence intensity of about 0.2–0.3%. The airfoil model was mounted horizontally across almost the entire width of the test section (1 mm gap on each side of the wind tunnel side window). In order to investigate the effect of the poro-serration on the aerodynamic forces, a 3-component strain gauge force balance was used to measure the lift and drag forces produced by the airfoil. As shown in Fig. 3b, it consists of a mounting plate, which is used to secure the device to the wind tunnel side window, and a triangular force plate. The force plate and the mounting plate were connected via three spherical universal joints constraining the motion of the force plate parallel to the direction of the mounting plate. Forces incurred by the airfoil were transmitted to three strain gauges via the cables. The angle of attack of the airfoil was rotated via a disc between 0° to 20°.

### III. Noise Results

Using a single far field microphone at polar angle of  $\theta = 90^\circ$  at a distance of 1.0 m from the airfoil trailing edge at mid span, the Sound Pressure Level (SPL) produced by the groups of serration (S0, S1, S1<sup>+</sup>) and (S0, S3, S3<sup>+</sup>) were measured at a velocity of  $U = 40 \text{ ms}^{-1}$ . These are shown in Figs. 4a–b respectively. The figures demonstrate that airfoil trailing edge serrations cut into the main body of the airfoil (S1, S3), or with the porous nickel-chromium foam filling the gaps between adjacent members of the sawtooth (S1<sup>+</sup>, S3<sup>+</sup>), have a substantial effect on the radiated noise spectra compared to the untreated baseline trailing edge S0. First, as expected, ‘tone’ is produced for both the S1 and S3 serrations due to the bluntness-induced vortex shedding in the wake. The tone produced by the S1 serrated trailing edge has a narrower frequency bandwidth and larger noise magnitude than that produced by the S3 serrated trailing edge, even though they share the same  $2h$  and  $\varepsilon$ . The peak frequency of the tone for both the S1 and S3 serrated trailing edges is roughly the same at 1 kHz. As previously explained in [7] the S1 serration has a greater number of “blunt roots” per unit span leading to greater spanwise coherence of the longitudinal vortex shedding for the narrower serration angle (compare Figs. 16b and 16c in [7]). Therefore a serrated trailing edge with a narrower serration angle, such as the S1 case, should produce a higher tone noise level.

At frequencies greater than 1 kHz (the vortex shedding frequency), both the S1 and S3 serrated trailing edges achieve substantial broadband noise reductions. In some cases, noise reduction in excess of 5 dB is observed at this particular velocity. The narrower serration is found to provide greater noise reductions than the wider serration,

consistent with the theoretical predictions of Howe [11]. In conclusion, therefore, a serration cut into the main body of an airfoil with a narrower serration angle provides better broadband noise reduction, but more intense tonal vortex shedding noise.

With porous nickel-chromium foam now introduced between adjacent teeth, both  $S1^+$  and  $S3^+$  porous-serrations not only *completely* suppress the bluntness-induced vortex shedding tonal noise, but also provide a *consistently lower* noise level compared to the baseline straight trailing edge  $S0$ . Comparing the poro-serrated trailing edge  $S1^+$  with its  $S1$  counterpart reveals similar levels of broadband noise reduction at frequencies,  $f$ , greater than about 1.7 kHz. In addition, the spectral shapes follow a similar frequency oscillation pattern at  $f > 1.7$  kHz. The same observation applies to the  $S3^+$  and  $S3$  trailing edges, where similar levels of broadband noise reduction are observed at  $f > 1.85$  kHz and both follow the same spectral shape.

Another advantage of introducing porous metal foam in the gaps between adjacent teeth is that high frequency noise increases, as observed by Gruber et al. [12] with the use of conventional flat plate type serrated trailing edge, is avoided. They attributed this noise increase to the presence of cross-jet through the gaps between adjacent teeth. However, with the introduction of metal foam now filling this gap, this mechanism is now avoided and no significant increase in noise is observed over the frequency range of interest up to 20 kHz.

The following sections will discuss more thoroughly the impact of introducing the ( $S1^+$ ,  $S3^+$ ) poro-serrated trailing edges to the airfoil self noise reduction.

### **A. Suppression of the Bluntness-Induced Vortex Shedding Tonal Noise**

The source of the vortex shedding tonal noise is located at the airfoil's near wake region [7] and hence a hot-wire probe was used to measure the wake flow in a two-dimensional  $y$ - $z$  plane at  $x/C = 1.03$  for the  $S0$ ,  $S1$  and  $S1^+$  trailing edges. The flow measurement was carried out *in situ* at the Brunel aeroacoustic wind tunnel, i.e., at the identical experimental condition to the noise measurements presented in Fig. 4a where  $U = 40 \text{ ms}^{-1}$ . The hot-wire measurements were made over the plane of  $(y, z) = (\pm 14 \text{ mm}, \pm 5 \text{ mm})$ , at a resolution of 0.5 mm in both directions. As shown in Fig. 5,  $z = -5, 0$  and  $5 \text{ mm}$  correspond to the tip of the sawtooth; whilst  $z = -2.5$  and  $2.5 \text{ mm}$  correspond to the root of the sawtooth, where  $y = 0$  corresponds to the trailing edge.

Figures 5a–c show contour maps of the fluctuating velocity power spectral density at a frequency of 1 kHz for the  $S0$ ,  $S1$  serrated and  $S1^+$  poro-serrated trailing edges, respectively. This frequency corresponds to the tonal peak produced by the  $S1$  serrated trailing edge as demonstrated in Fig. 4a. For the  $S0$  baseline case, where no tone noise



is observed, the fluctuating velocity spectrum is uniform across the spanwise ( $z$ ) direction. However, for the nonflat plate S1 serrated trailing edge in Fig. 5b, the level of velocity fluctuation is much higher. Large velocity fluctuation can also extend to the otherwise freestream region ( $y > 12 \text{ mm} \in y < -12 \text{ mm}$ ). The large velocity fluctuation is seen to be fairly uniform across the  $z$  direction, thus lending further support to the notion that stronger coherent vortex shedding can be produced by a narrow angle serrated trailing edge.

As soon as the gaps between adjacent members of the sawtooth are filled with the porous metal foams (S1<sup>+</sup>), Fig. 5c indicates that the fluctuating velocity *PSD* contour map becomes almost identical with that produced by the baseline S0 trailing edge. The only exception is that the S1<sup>+</sup> poro-serrated trailing edge produces extra feature comprising two narrow and wavy lines of turbulent structures mirrored at around the  $y = 0$  line. These are likely to be caused by the rough surface of the porous metal foams where the turbulence level of the near wall boundary layer is enhanced. Based on the geometry of the S1<sup>+</sup> poro-serrated trailing edge, if the effective length of the porous material at a specific  $z$  location is denoted by  $l_p(z)$ , then  $l_p(z) = (\tan\phi)^{-1}z$ , where  $0 < z < \pm 2.5 \text{ mm}$ . The waviness of the turbulent structures is therefore due to the periodic variation of  $l_p(z)$ , i.e. maximum near the sawtooth roots ( $z = \pm 2.5 \text{ mm}$ ) but minimum at the sawtooth tip ( $z = 0, \pm 5 \text{ mm}$ ). Note that footprints of these wavy turbulent structures could persist up to  $f \approx 10 \text{ kHz}$ .

The overall wake power spectral density at a particular  $z$  location,  $\Phi(z, f)$ , can be estimated from:

$$\Phi(z, f) = 10 \log_{10} \int \phi'(y, z, f) dy \quad (1)$$

where  $\phi'(y, z, f)$  is the mean square fluctuating velocity in the wake flow. Figures 6a–e compare the  $\Phi(z, f)$  for the S0, S1 and S1<sup>+</sup> serrations at  $z = 0$  (tip),  $z = 1 \text{ mm}$ ,  $z = 2.5 \text{ mm}$  (root),  $z = 4 \text{ mm}$  and  $z = 5 \text{ mm}$  (tip), respectively. All the S0, S1 and S1<sup>+</sup> *PSD* feature the same high frequency roll-off of  $f^{-5/3}$ , indicating that the wake flow is turbulent. The dominant narrowband peaks in the wake for the S1 serrated trailing edge, which occur at approximately 1 kHz, match exactly the acoustic tones measured by the free field microphone in Fig. 4a. When the serrated trailing edge is replaced by the S1<sup>+</sup> poro-serration the narrowband peaks in the wake are completely suppressed across the whole range of  $z$ . The  $\Phi$  levels produced by the S0 baseline, S1 serrated and S1<sup>+</sup> poro-serrated trailing edges are quite similar beyond the tone frequency (i.e.  $f > 1 \text{ kHz}$ ), especially close to the sawtooth tip at  $z = 0$  and 5 mm. However, near the sawtooth root region of  $z = 2.5 \text{ mm}$ , both the S1 serrated and S1<sup>+</sup> poro-serrated trailing edges produce slightly higher  $\Phi$  level than the S0 case at  $f > 1.5 \text{ kHz}$ . This is likely to be caused by the largest bluntness at this

particular  $z$  location for the S1 serrated trailing edge (hence the strongest vortex shedding), and the largest  $l_p(z)$  for the poro-serrated trailing edge (hence the strongest turbulence level of the near wall boundary layer). Nevertheless, the higher near wake  $\Phi$  level at the serration root region does not compromise the trailing edge noise reduction capabilities of the S1 serrated and S1<sup>+</sup> poro-serrated trailing edges.

## B. Broadband Noise Reduction

In the previous section, only noise results at  $U = 40 \text{ ms}^{-1}$  were presented. Here we examine the performance matrix of the serrated trailing edges at other velocities. The difference in Sound Pressure Level ( $\Delta\text{SPL}$ ) between a baseline, straight trailing edge (S0) and the serrated trailing edges (S1, S1<sup>+</sup>, S3 and S3<sup>+</sup>) can be calculated as

$$\Delta\text{SPL}(U, f) = \text{SPL}_{\text{baseline}}(U, f) - \text{SPL}_{\text{serration}}(U, f) \quad (2)$$

Figures 7a and 7b, and 8a and 8b show contour maps of  $\Delta\text{SPL}$  as a function of frequency and mean velocity ( $U = 20\text{--}60 \text{ ms}^{-1}$ ) for the S1 and S1<sup>+</sup> serrations, and for the S3 and S3<sup>+</sup> serrations, respectively. Note that the velocity resolution in these figures is  $2 \text{ ms}^{-1}$ . The same resolution also applies to other  $\Delta\text{SPL}$  contour maps throughout the paper. For the serrated trailing edges S1 and S3 in Figs. 7a and 8a, significantly Strouhal-dependent tonal ‘rungs’ over a narrowband frequency range (light blue to dark blue colors) are accompanied by substantial turbulent broadband noise reduction over a larger frequency range (yellow to red colors). The lower and upper limits of the tonal rungs in Figs. 7a and 8a are found to scale with  $0.12 < St_\varepsilon < 0.22$ , where  $St_\varepsilon$  is the Strouhal number based on the serration bluntness  $\varepsilon$ . The level of bluntness-induced vortex shedding noise becomes less significant as the serration angle increases. The level of broadband noise reduction also reduces as the serration angle increases. This phenomenon has been reported in our previous works in [7].

As shown in Figs. 7b and 8b, the current work represents a substantial improvement in noise control performance in that the tonal rungs can now be completely suppressed by the addition of porous metal forms in the gaps between the teeth, whilst the efficiency of broadband noise reduction is largely preserved. Within the velocity range under investigation here, up to 7 dB broadband noise reduction can be achieved.

A conventional delay-and-sum beamformer was used to confirm that the measured airfoil radiation originates from the trailing edge. The plane of the array was held below the airfoil and the beam scanned over the plane of the airfoil. Figure 9a shows the noise map corresponding to the baseline, S0 case at  $U = 40 \text{ ms}^{-1}$ . The beamformer map

is shown at a single frequency of 2.3 kHz, which corresponds to the centre of the frequency band where most of the broadband noise reduction occurs (see Fig. 4a). Figure 9a shows conclusively that the broadband noise at this frequency, as seen from the previous noise spectra measured by a single microphone in Fig. 4a, mainly originated from the straight trailing edge of the airfoil. In Fig. 9b, where the trailing edge is now replaced with the S1<sup>+</sup> porous-serration type, the noise map demonstrates a significantly reduced level of broadband noise radiation from the trailing edge by more than 5 dB.

As mentioned in Section II, an identical experiment has been performed in the open jet wind tunnel rig at the ISVR, University of Southampton for repeatability test. Figures 10a and 10b show the corresponding contour maps of  $\Delta$ SPL, as a function of frequency and mean velocity ( $U = 20\text{--}60 \text{ ms}^{-1}$ ), for the S3 serrated and S3<sup>+</sup> poro-serrated trailing edges, respectively. Comparing Figs. 8a–b and Figs. 10a–b shows good repeatability of the noise performance by the S3 and S3<sup>+</sup> trailing edges. The tonal rung produced by the S3 serrated trailing edge is also found to scale with  $0.12 < St_e < 0.22$ . The capabilities of the poro-serrated trailing edge to completely suppress bluntness-induced vortex shedding noise, and significantly reduce broadband noise, have been re-confirmed in this repeatability test.

### C. Mechanism of Broadband Noise Reduction by the Poro-Serrated Trailing Edges

Fully porous of the whole airfoil has been shown to afford significant broadband noise reduction [4]. However, by making the whole airfoil fully porous the overall lift is reduced and drag is increased. In order to recover some of the aerodynamic performance for a fully porous airfoil, Geyer and Sarradj [13] used a thin PVC film to cover the main part of the airfoil body, thereby exposing only a partially porous trailing edge. If  $s$  denotes the chordwise extent of the porous trailing edge, Geyer and Sarradj investigated the partial porous airfoil in the range of  $0.05 < s/C < 0.5$ . They observed that broadband noise can still be reduced by the partially porous trailing edge, which they attributed to the damping of the hydrodynamic pressure fluctuations by the porosity at the trailing edge.

The S1<sup>+</sup> and S3<sup>+</sup> poro-serrated trailing edges investigated in this study utilize porous nickel-chromium foams to fill the gaps between adjacent members of the sawtooth. As illustrated in the drawings in Table 1, the S1<sup>+</sup> and S3<sup>+</sup> poro-serrated trailing edge exhibit a spanwise interchanging of solid–porous interfaces, i.e. the nonporous, solid sawtooth structure and the porous metal foams at the interstices both occupy approximately the same surface area per unit span. We now seek to determine whether the broadband noise reduction obtained using the S1<sup>+</sup> and S3<sup>+</sup> poro-serrated trailing edges is due to the serration or the porous material, or both. To do this, two different types of

trailing edge devices were manufactured and their noise spectra were measured under the same flow condition as the  $S1^+$  and  $S3^+$  cases.

The first trailing edge device is referred to as  $S3^-$  ‘inversed poro-serrated’ trailing edge, which is the inverted version of the  $S3^+$  poro-serrated trailing edge. As illustrated in Table 1, the sawtooth structure is now replaced with porous nickel-chromium foam, whilst the sawtooth gaps (interstices) are filled with solid, nonporous object. The corresponding noise map of  $\Delta\text{SPL}$  versus frequency and flow speed is shown in Fig. 11. Because there is also no blunt surface exposure for the  $S3^-$  trailing edge, the absence of the bluntness-induced vortex shedding tonal noise is expected. However, it is observed that the  $S3^-$  “inversed poro-serrated” trailing edge is less effective than the  $S3^+$  poro-serrated trailing edge in broadband noise reduction. Comparing Fig. 8b and Fig. 11 reveals that noise reduction achieved by the  $S3^-$  “inversed poro-serrated” trailing edge only occurs at a much lower frequency than the  $S3^+$  poro-serrated trailing edge, and the frequency bandwidths are also smaller. In addition, as demonstrated by the large region of negative  $\Delta\text{SPL}$ , the  $S3^-$  trailing edge produces higher noise level than the baseline  $S0$  trailing edge at  $f > 1$  kHz across the whole velocity range. Therefore the overall noise performance of the  $S3^-$  trailing edge is not satisfactory. Further discussion of the  $S3^-$  “inversed poro-serrated” trailing edge will be provided in Section V.

The second trailing edge device under investigation here is denoted as SP. This trailing edge device is formed by machine cutting a large piece of porous nickel-chromium foam to produce a continuous trailing edge profile, which is then attached to the solid airfoil main body, thus resembling the partially porous, straight trailing edge concept of Geyer and Sarradj [13]. Note that the SP partially porous trailing edge does not contain any serration pattern. In order to maintain an exactly same  $2h$  as the  $S1^+$  and  $S3^+$  poro-serrated trailing edges, the porous nickel-chromium foam section of SP is  $s = 20$  mm. The corresponding noise map of  $\Delta\text{SPL}$  versus frequency and flow speed for the SP partially porous trailing edge is shown in Fig. 12. Noise reductions are seen to be limited to the higher flow speeds of  $U > 30 \text{ ms}^{-1}$ . At  $f > 8$  kHz, at all velocities, noise is observed to increase which is likely to be caused by the surface roughness of the porous metal foams. Also present in the noise map is a weak, narrowband ‘rung’ which scales with  $0.15 < St_\varepsilon < 0.18$ , where  $\varepsilon$  is the same value as the  $S1$  and  $S3$  serrated trailing edges. The close resemblance of the Strouhal number dependencies between the  $S1$ ,  $S3$  serrated trailing edges and the SP partial porous trailing edge for the tonal rungs suggests that they all share the same vortex shedding noise source from the blunt roots (at  $x/C = 0.87$ ). Fluid flowing through the SP trailing edge at  $x/C = 0.87$ , which is the interface between the solid main body and the porous trailing edge, could result in reasonably strong longitudinal vortex shedding for

the radiation of tonal noise. On the other hand, the  $S1^+$  and  $S3^+$  poro-serrated trailing edges (also the  $S3^-$  “inversed poro-serrated” trailing edge) are far more effective in suppressing the vortex shedding noise. This is likely to be caused by the presence of spanwise interchanging of solid–porous interface near the trailing edge to inhibit the development of the longitudinal vortex shedding with strong spanwise coherence.

To summarize, both the SP partially porous trailing edge and  $S3^-$  “inversed poro-serrated” trailing edge are only effective in noise reduction at low frequencies with a narrow bandwidth. This is markedly different if compared with the  $S1$ ,  $S1^+$ ,  $S3$  and  $S3^+$  serrated trailing edges, which all have demonstrated more superior noise reduction capabilities. The  $S3^-$  “inversed poro-serrated” trailing edge contains the same amount of porous nickel-chromium foams as the  $S3^+$  poro-serrated trailing edge per unit span, and yet it only matches in noise reduction capability as the partially porous SP trailing edge that does not feature sawtooth serration at all. Therefore, there is strong evidence that the broadband noise reduction achieved by the  $S1^+$  and  $S3^+$  poro-serrated trailing edges is mainly caused by the effect of sawtooth serration. However, we also have evidences to prove that the porous material filling the sawtooth gaps, if selected properly, could also contribute in further reduction of broadband noise level. The result will be presented next.

#### **D. Other porous materials in the “Poro”-Serrated Trailing Edge**

In previous sections, the porous material employed by the poro-serrated trailing edge is the nickel-chromium foams. This section will investigate the characteristics in broadband noise reduction when different porous materials are used to fill the gaps between the sawtooth. The first is referred to here as the  $S3^\Delta$  serration, and its drawing can be found in Table 1. This configuration comprises a thin layer of brushes in place of the porous nickel-chromium foam to lightly fill the gaps between adjacent members of the  $S3$  sawtooth. The corresponding noise map of  $\Delta$ SPL versus frequency and mean flow speed is shown in Fig. 13. By comparing Fig. 8b and Fig. 13, the  $S3^\Delta$  serrated trailing edge is seen to be as effective as the  $S3^+$  poro-serrated trailing edge in suppressing vortex shedding tonal noise. Moreover, the frequency range over which broadband noise reduction achieved by the  $S3^\Delta$  serrated trailing edge is even found to be slightly wider than the  $S3^+$  poro-serrated trailing edge, especially in the mid to higher velocity regions.

Note that the brushes in the  $S3^\Delta$  serrated trailing edge must be relatively thin. If the brush density at each sawtooth gap is too high, the effectiveness of the broadband noise reduction will be negated. At the same time, a

noticeable level of noise increase at high frequency is also observed. This behavior is reflected in Figs. 14a–c for the noise spectra measured at  $U = 40 \text{ ms}^{-1}$  by the  $S3^\Delta$  serrated trailing edge with “high-density”, “medium-density” and “light-density” brushes at the sawtooth gaps. Note that the “medium-density” and “light-density” brushes are approximately 60% and 30%, respectively, of the “high-density” brush. The results demonstrate that the overall noise performance improves as the brush density reduces.

The above observations of wider frequency range of  $+\Delta\text{SPL}$  (broadband noise reduction) achieved by  $S3^\Delta$ , and the dependence of brush density in the overall noise performance strongly suggest that the porous material on the sawtooth gaps could also play a positive role in the turbulent broadband noise reduction.

Next, the porous nickel-chromium foam for the  $S3^+$  poro-serrated trailing edge is replaced with Melamine foam, and the new combination is called  $S3^{++}$  poro-serrated trailing edge. Note that both the  $S3^+$  and  $S3^{++}$  poro-serrated trailing edges share exactly the same sawtooth geometry. Figure 15a shows the comparison of SPL between the  $S3^+$  and  $S3^{++}$  poro-serrated trailing edges at  $U = 36 \text{ ms}^{-1}$ . It can be seen that the  $S3^{++}$  poro-serrated trailing edge can also completely suppress the vortex shedding tonal noise. Most importantly, it outperforms the  $S3^+$  counterpart in the level of broadband noise reduction across a wide range of frequency, except in the frequency range of  $1.5 \text{ kHz} < f < 2.2 \text{ kHz}$  where both the  $S3^+$  and  $S3^{++}$  produce equal SPL.

Figure 15b shows contour map of  $\Delta\text{SPL}$  as a function of frequency and mean velocity for  $(\text{SPL}_{S3^+} - \text{SPL}_{S3^{++}})$ . A positive value denotes that the  $S3^{++}$  poro-serrated trailing edge produces lower level of noise radiation compared to the  $S3^+$  counterpart, and vice versa. It can be seen that the contour map is dominated by positive values of  $\Delta\text{SPL}$  (+1 to +2 dB) across the frequency and velocity domains. Because the sawtooth geometries for both the  $S3^+$  and  $S3^{++}$  poro-serrated trailing edge are exactly the same, a nonzero value in  $\Delta\text{SPL}$  in this case must be related to the choice of the porous material at the sawtooth gaps. Many parameters can be used to describe a porous material, such as the air flow resistivity, permeability, density, surface roughness, pore/cell size and number of pores per unit area, but which of these is the main mechanism causing the  $S3^{++}$  poro-serrated trailing edge to achieve better noise performance remains a subject of investigation in the future.

#### IV. Aerodynamic Performance

As discussed in Section I most of the early serrated trailing edges have been in the form of flat plate inserts. However, the artificial lengthening of the airfoil geometry could affect the global flow circulation around it, thus possibly leading to modification in the aerodynamic performance.

The proposed nonflat plate type serrated trailing edge preserves the original airfoil shape with the advantage that aerodynamic performance is not compromised significantly. This section will investigate the effect of these various serrations on the lift coefficient (CL) and drag coefficient (CD) of the NACA0012 airfoil with the S1<sup>+</sup> and S3<sup>+</sup> poro-serrated trailing edges from 0° to 20° angle of attack ( $\alpha$ ). As mentioned in Section II force measurements were carried out in a wind tunnel with a closed-test section. Flow conditions are therefore different from the open jet wind tunnel used for the noise test but are still useful for assessing changes in the aerodynamic performance. The velocity of the wind tunnel was set at 30 ms<sup>-1</sup> during the force measurement. For consistency the tripping elements near the airfoil's leading edge on both sides were retained.

Figure 16a presents the lift coefficients CL versus angle of attack  $\alpha$  for the S0, S1<sup>+</sup> and S3<sup>+</sup> trailing edges. For the baseline S0 trailing edge, CL increases linearly with  $\alpha$  at a rate of approximately 0.1 per degree up to  $\alpha = 5^\circ$ . Above this angle, the CL increases at a slower rate and deviates from the thin airfoil theory. This may be due to the thickening of the boundary layer at the airfoil's suction side and the viscous effects. The CL<sub>max</sub> is seen to occur at  $\alpha \approx 12^\circ$ , beyond which the CL drops significantly, reaching a plateau at  $14^\circ \leq \alpha \leq 20^\circ$ . When the airfoil is replaced with the S1<sup>+</sup> and S3<sup>+</sup> poro-serrated trailing edges, the variations in CL are similar to the S0 baseline case up to  $\alpha \approx 8^\circ$ . At angles  $8^\circ \leq \alpha \leq 12^\circ$  (before the stall angle), the S1<sup>+</sup> and S3<sup>+</sup> poro-serrated trailing edges start to produce approximately 4% lower CL than the baseline S0 trailing edge. The S1<sup>+</sup> and S3<sup>+</sup> poro-serrated trailing edges continue to underperform at the post-stall regime, with the CL now reduced by up to 10% compared to the baseline S0 case.

Figure 16b presents the drag coefficient CD versus  $\alpha$  for the S0, S1<sup>+</sup> and S3<sup>+</sup> trailing edges. The CD values are generally high because the boundary layers near the leading edge were tripped into turbulent. For the S0 baseline trailing edge, the linearity of CD with  $\alpha$  is also observed up to  $\alpha = 5^\circ$ . The stall angle at  $\alpha = 12^\circ$  is accompanied by a significant increase in CD. As expected, CD then further increases at a higher rate with  $\alpha$  at the post-stall regime. We first examine the effect on CD by the S3<sup>+</sup> porous-serration. Despite the increased surface roughness due to the

porous metal foams, CD associated with the S3<sup>+</sup> poro-serrated trailing edge follows almost exactly the same trend as the baseline S0 trailing edge throughout the pre-stall, and post-stall regimes up to  $\alpha = 14^\circ$ . At  $\alpha > 14^\circ$ , the S3<sup>+</sup> poro-serrated trailing edge even produces lower CD than the baseline S0 case. This phenomenon is further replicated by the S1<sup>+</sup> poro-serrated trailing edge. Notwithstanding the same CD values produced at  $0^\circ \leq \alpha \leq 14^\circ$ , the S1<sup>+</sup> poro-serrated trailing edge performs better than the S0 trailing edge at  $\alpha > 14^\circ$ , affording a maximum of 6% lower drag.

What causes the poro-serrated trailing edge to produce lower lift and lower drag than the straight trailing edge at the post-stall regime remains unclear. One possible explanation is that the porous material near the trailing edge allows “communication” of boundary layers between the suction side and pressure side. Such a communication will cause an overall reduction in thickness of the shear layer leaving the trailing edge, hence the drag, as a result of flow dissipations through the porous metal foams. Similarly, the communication of boundary layers between the suction side and pressure side might displace the aft stagnation point, which could lead to a change of flow circulation around the airfoil, hence the lift. Note that these conjectures only apply to very large angle of attack cases when the pressure difference across the porous metal foams near the trailing edge is also large.

Another useful parameter used to examine the aerodynamic performance of the serrated airfoil is the lift-to-drag ratio (CL/CD). A large value of CL/CD is desired as it entails the maximum lift force generation with minimal drag penalty. Figure 16c shows the CL/CD versus  $\alpha$  for the S0, S1<sup>+</sup> and S3<sup>+</sup> trailing edges. For the baseline S0 trailing edge, the ratio CL/CD increases steadily with  $\alpha$ , reaching a maximum value at  $\alpha = 6^\circ$ . Between  $6^\circ \leq \alpha \leq 9^\circ$ , CL/CD falls steadily. After that the CL/CD undergoes a significant drop at  $\alpha = 10^\circ$ . A second significant drop happens again at  $\alpha = 12^\circ$ , corresponding to the stall angle. At  $\alpha > 12^\circ$ , at the post-stall regime, the CL/CD steadily declines with  $\alpha$ . Examination of the S3<sup>+</sup> poro-serrated trailing edge reveals that its CL/CD is consistently lower than the baseline S0 case. The largest discrepancy occurs at  $4^\circ \leq \alpha \leq 9^\circ$ , where up to a 17% difference is obtained. However, the S1<sup>+</sup> poro-serrated trailing edge, which has a narrower serration angle, recovers its CL/CD to almost the same level as the baseline S0 trailing edge throughout the range of  $\alpha$  in both the pre-stall and post-stall regimes. The remarkable recovery of CL/CD by the S1<sup>+</sup> poro-serrated trailing edge is thus very encouraging.

Although the aerodynamic results provided in this section are far from exhaustive, they suggest that the best recovery of the aerodynamic performances for a poro-serrated trailing edge is related to the one with the smallest serration angle  $\phi$ . This finding could have anticipated because the smallest serration angle entails a more significant discontinuity of the porous metal foams in the spanwise direction, and that a constant porous medium as part of an



airfoil is likely to be more detrimental for its aerodynamic forces. Remarkably, the criterion of low serration angle  $\phi$  for maintaining the aerodynamic performances is the same for achieving the optimal broadband noise reduction.

## V. Discussions

Sections III.A and III.B of this paper have demonstrated the capability of the  $S1^+$  and  $S3^+$  poro-serrated trailing edges to completely suppress vortex shedding tonal noise that would otherwise be produced by the  $S1$  and  $S3$  serrated trailing edges, whilst at the same time maintaining the same level of broadband noise reduction. We have confirmed that broadband noise reductions by the  $S1^+$  and  $S3^+$  poro-serrated trailing edges are mainly caused by the serration effect (in Section III.C), even though by filling the gaps between adjacent members of the sawtooth in  $S1^+$  and  $S3^+$  a seemingly “straight” trailing edge is formed (see Figs. 17a–b). However, further question remains for the increased surface roughness introduced by the porous nickel-chromium foams and its implication to the noise radiation.

To address these issues two surface-mounted hot-film sensors (HF1 and HF2) were located onto the baseline  $S0$ , and the  $S3^+$  poro-serrated trailing edges at  $x/C \approx 0.95$  but spaced 6 mm apart ( $\Delta z$ ) in the spanwise direction. This spanwise spacing for the  $S3^+$  poro-serrated trailing edge is designed such that one hot-film sensor (HF1) is situated within the solid, nonporous sawtooth surface, while another hot-film sensor (HF2) is situated within the porous metal foam, as illustrated in Fig. 17b. The exact locations of HF1 and HF2 in the  $S3^+$  poro-serrated trailing edge are replicated in the  $S0$  straight trailing edge (Fig. 17a), though both hot-film sensors are now situated on the solid surface.

Figure 18 shows the drawing of a surface-mounted hot-film sensor. The sensing element of the hot film sensor is deposited on a thin Kapton foil, which can completely isolate the hot-film sensing element and the underneath porous surface. Therefore the hot-film sensor is only sensitive to the longitudinal velocity fluctuation at the near wall boundary layer, and it cannot register any cross flow component directly through the porous nickel-chromium foam. The extended Kapton foil within the dotted box area, as indicated in the drawing, was removed before the hot film sensor was glued on the surface. As a result, the sensing element is approximately 1.5 mm behind the edge of the Kapton foil. This shortened buffer length allows the natural mixing between the upstream cross flow component through the nickel-chromium foam and the upstream boundary layer, and yet it can also prevent the cross flow component from reaching the sensing element directly.

The fluctuating signals measured by the hot-film sensor are non-dimensionalized by their standard deviation values, respectively. Figure 19a shows the corresponding power spectral densities measured by the HF1<sub>S0</sub> and HF1<sub>S3<sup>+</sup></sub> sensors at  $U = 40 \text{ ms}^{-1}$ . Note that the subscript denotes a particular type of trailing edge used. The mid-frequency and high-frequency roll-off of approximately  $f^{-5/3}$  and  $f^{-5}$ , respectively, for both HF1<sub>S0</sub> and HF1<sub>S3<sup>+</sup></sub> suggest that the turbulent boundary layer is fully developed (this might only be true at  $x/C = 0.95$ . As shown in [14], the existence of some oblique vortical structures along the side edges of the solid-surfaced sawtooth is likely to yield a different PSD characteristic if  $x/C$  is closer to unity, i.e. towards the sawtooth tip). On the other hand, as shown in Fig. 19b, HF2<sub>S3<sup>+</sup></sub> (situated on the porous surface) produces slightly lower spectral level at low frequency, but considerably higher level at  $f > 2.2 \text{ kHz}$ , than the HF2<sub>S0</sub> counterpart.

Measurements of the surface-mounted hot-film signals were also performed at  $20 \leq U \leq 60 \text{ ms}^{-1}$ . The following parameter is introduced:

$$\Delta \xi_i(U, f) = \xi_{i_{S0}}(U, f) - \xi_{i_{S3^+}}(U, f), \quad (3)$$

where  $\xi$  is the power spectral density level measured by a particular type of hot-film sensor,  $i = 1$  or  $2$ , for either the S0 and S3<sup>+</sup> trailing edges.  $\Delta \xi_1$  is designed to show the difference in power spectral density levels between HF1<sub>S0</sub> and HF1<sub>S3<sup>+</sup></sub>, where both hot-film sensors are situated on solid surfaces. Likewise,  $\Delta \xi_2$  will show the difference in power spectral density levels between HF2<sub>S0</sub> and HF2<sub>S3<sup>+</sup></sub>, but the HF2<sub>S0</sub> is situated on a solid surface and the HF2<sub>S3<sup>+</sup></sub> is on a porous surface. The largely zero value of  $\Delta \xi_1$  in Fig. 20a confirms that both the power spectral densities at locations HF1<sub>S0</sub> and HF1<sub>S3<sup>+</sup></sub> are similar throughout the frequency–velocity domain. However, the  $\Delta \xi_2$  contour in Fig. 20b is noticeable different. Three distinct zones can be identified from Fig. 20b:

1. Zone I (low frequency range) has a slight positive level of  $\Delta \xi_2$  up to 2 dB.
2. Zone II (mid frequency range) contains the  $\Delta \xi_2$  which is largely close to zero value.
3. Zone III (high frequency range) is characterized by a considerable negative level of  $\Delta \xi_2$  up to –6 dB.

A predominantly negative level of  $\Delta \xi_2$  in Zone III implies that the porous surface produces higher power spectral density level than the solid, nonporous surface. We now assume that the power spectral density measured by the hot-film sensors near the trailing edge shares a close causality with the radiated noise spectrum. The negative level of  $\Delta \xi_2$  in Zone III could translate to a noise increase by the S3<sup>+</sup> poro-trailing edge at high frequency. A positive level of

$\Delta\xi_2$  in Zone I (low frequency range) would suggest that noise reduction is possible. Likewise, a zero level of  $\Delta\xi_2$  in Zone II (mid frequency range) could stipulate an unchanged noise level. To verify the above conjectures, Zones I, II and III identified from Fig. 20b are now embedded into the  $\Delta\text{SPL}$  contour map in Fig. 20c for the  $S3^+$  poro-serrated trailing edge. The following summarizes the outcomes of the comparison:

1. The negative level of  $\Delta\xi_2$  in Zone III does not result in significant noise increase at the same zone.
2. Noise reduction at Zone I is not realized despite the slight positive level of  $\Delta\xi_2$  at the same zone.
3. Most crucially, most of the broadband noise reduction observed in the  $\Delta\text{SPL}$  actually occurs at Zone II, where the level of  $\Delta\xi_2$  at the same zone is largely zero.

In summary, none of the initial conjectures are true regarding the effect of porous metal foams to the radiated noise. Despite that the porous metal foam will increase the overall ‘roughness’ of the trailing edge surface, it does not seem to cause noise increase at high frequency, nor to achieve significant noise reduction at low frequency. The primary effect of the porous metal foams exerting on the overall noise radiation for the  $S3^+$  poro-serrated trailing edge is to undermine the bluntness exposed by the serration roots, thus avoiding the vortex shedding tonal noise. Despite that the addition of the porous metal foam will cause the trailing edge appearing ‘straight’, it does not enhance the scattering efficiency that one would expect from a straight, unserrated trailing edge. Therefore the broadband noise reduction observed in the  $\Delta\text{SPL}$  contours for the  $S1^+$  and  $S3^+$  poro-serrated trailing edges is primarily caused by the serration effect. Although the hot-film test was not carried out for the  $S3^{++}$  poro-serrated trailing edge, the mechanism is expected to be the same.

Finally, the results presented thus far could provide a hint about the mechanism underpinning the broadband noise reduction by the  $S1^+$  and  $S3^+$  poro-serrated trailing edges. Table 2 summarizes the  $\Delta\text{SPL}(f, U)$  for the  $S3$ -type trailing edges ( $S3$ ,  $S3^+$ ,  $S3^-$ ,  $S3^A$  and  $S3^0$ ), as well as the  $SP$ . In the table, Zones I, II and III identified from the  $\Delta\xi_2(f, U)$  contour in Fig. 20b are also superimposed in each of the  $\Delta\text{SPL}(f, U)$  contour maps. It is clear that the  $\Delta\text{SPL}(f, U)$  associated with the above trailing edge devices could be categorized into two distinct groups (Group A and Group B). The  $S3$ ,  $S3^+$  and  $S3^A$  trailing edges belong to Group A, from which significant broadband noise reduction is achieved at Zone II. On the other hand, the Group B trailing edges ( $S3^-$ ,  $S3^0$  and  $SP$ ) could only produce noise reductions in the lower frequency region of Zone I. The frequency bandwidth is also narrower, and these trailing

edges seem to be only effective at  $U > 30 \text{ ms}^{-1}$ . In addition, noticeable level of noise increase actually occurs in most of Zone III, and in one case occurs in Zone II by the SP trailing edge. Therefore, the fluctuating velocity power spectral density in the  $\Delta\xi_2$  contour (Fig. 20b) share a better correlation with the  $\Delta\text{SPL}$  noise performance produced by the Group B trailing edges, but not with the poro-serrated trailing edge which belongs to Group A. This suggests that any property changes in the trailing edge by the porous material (e.g. air flow resistivity, permeability and surface roughness) is not the primary reason for the broadband noise reduction in Zone II.

A common feature of the Group A trailing edges ( $S3$ ,  $S3^+$  and  $S3^A$ ) is that their sawtooth serrations are made from nonporous, solid surfaces. Likewise, the sawtooth serrations in Group B ( $S3^-$  and  $S3^o$ ), including a partially porous, unserrated trailing edge in the SP case, are made from porous metal foam. Such distinction stipulates that an effective broadband noise reduction would require the sawtooth serrations to be made from solid surface. It remains an interesting question that a sawtooth serration made from porous metal foams, even if it shares the same geometrical parameters as the sawtooth surface made from solid surface, could not demonstrate a similar capability in broadband noise reduction. The answer may be related to the acoustical scattering efficiency of the turbulent wavenumber components on a porous sawtooth serration. This conjecture provides an avenue for further research to understand the trailing edge noise reduction mechanism by the serration technique.

## VI. Conclusions

This paper reports an experimental study on the aeroacoustic properties of a NACA0012 airfoil with a number of trailing edge devices ( $S1$ ,  $S1^+$ ,  $S3$ ,  $S3^+$ ,  $S3^{++}$ ,  $S3^-$ ,  $S3^A$ ,  $S3^o$  and SP). In particular, the poro-serrated trailing edges  $S1^+$ ,  $S3^+$ ,  $S3^{++}$  and  $S3^A$  represent the core of investigation. All these trailing edge devices, when integrated to an airfoil body, will retain the original airfoil shape and offer better structural stability than the conventional, flat plate type serrated trailing edge. The main objective of this work is to investigate whether it is feasible to employ these new trailing edge devices to reduce the turbulent broadband noise produced by the trailing edge of an airfoil. The free field noise measurements, as well as the wake flow measurement, were carried out inside an aeroacoustic wind tunnel facility at Brunel University London. The range of jet speeds under investigation was between  $20 \text{ ms}^{-1}$  and  $60 \text{ ms}^{-1}$ , corresponding to Reynolds numbers based on airfoil chord of  $2 \times 10^5$  and  $6 \times 10^5$  respectively. The lift and drag forces produced by the airfoil when fitted with the poro-serrated trailing edges were measured in a separate aerodynamic wind tunnel.

The use of S1 and S3 serrated trailing edges will result in sound pressure level reduction of the broadband noise up to 7 dB. However, noise increase caused by the vortex shedding from the exposed blunt roots is also very significant, especially for the S1 case. The use of porous nickel-chromium foams to fill the gaps between adjacent members of the sawtooth, as demonstrated by the  $S1^+$  and  $S3^+$  poro-serrated trailing edges, can completely suppress the vortex shedding tonal noise, whilst the level of broadband noise reduction remains the same. These poro-serrated trailing edges also demonstrated an excellent repeatability in noise performance when they were tested in another aeroacoustic facility. There is little aerodynamic penalty if these poro-serrated trailing edges are integrated to the airfoil body. Another benefit these poro-serrated trailing edges exhibits over the flat plate type serrated trailing edge is the minimal noise increase at high frequency. A trend discernible from the current results is that the  $S1^+$  poro-serrated trailing edge (with a narrower serration angle) performs better acoustically and aerodynamically than the  $S3^+$  counterpart. Both have the same root-to-tip distance ( $2h$ ).

Although not shown in this paper for clarity, an exactly similar outcome of the broadband noise reduction can be achieved by these poro-serrated trailing edges when the airfoil is adjusted to non-zero angles of attack, i.e.  $0.8^\circ$  and  $2.8^\circ$  effective angles of attack after applying the corrections of the jet nozzle height.

Another promising concept developed in this study is the  $S3^\Delta$  poro-serrated trailing edge where the gaps between adjacent members of sawtooth were partially filled with thin brushes instead of the porous nickel-chromium foams. The levels of noise reduction for both the vortex shedding tonal noise and the turbulent broadband noise are similar compared to the  $S3^+$  poro-serrated trailing edge. More interestingly, the  $S3^\Delta$  poro-serrated trailing edge achieves broadband noise reduction over a wider bandwidth in frequency than the  $S3^+$  counterpart, especially at higher velocity.

Two possible broadband noise reduction mechanisms could be associated with the poro-serrated trailing edges. One associated with the oblique edges due to the serrations, and the other arising from porosity which allows the pressure side and suction side to ‘communicate’ therefore reducing the acoustic dipole strength at the trailing edge. As discussed in Section III.C, whilst the SP,  $S1^+$  and  $S3^+$  trailing edges all used the porous nickel-chromium foams with the same porous length  $s$ , or serration root-to-tip distance  $2h$ , the partial porous trailing edge SP produces very different  $\Delta$ SPL characteristics when compared to the  $S1^+$  and  $S3^+$  poro-serrated trailing edges. Most importantly, the SP trailing edge could not match the level and bandwidth of broadband noise reduction achieved by the  $S1^+$  and  $S3^+$  poro-serrated trailing edges. Therefore there are clear evidences that the main mechanism underpinning the turbulent

broadband noise reduction by a poro-serrated trailing edge should come from the sawtooth serration effect. The porous nickel-chromium foam, on the other hand, is very effective in undermining the bluntness exposed by the serration roots, thus suppressing the vortex shedding tonal noise. The interesting outcome of the  $S3^{\Delta}$  serrated trailing edge encourages a further study to replace the porous nickel-chromium foam with Melamine foam at the sawtooth gaps. This new combination of the poro-serrated trailing edge ( $S3^{++}$ ) is found to achieve even greater level of broadband noise reduction than the  $S3^{+}$  counterpart. Based on all the evidences, whilst the main mechanism underpinning the broadband noise reduction of a poro-serrated trailing edge comes from the sawtooth serration, the porous material used to fill the sawtooth gaps has a potential to further reduce the turbulent broadband noise level.

For all the trailing edge devices investigated in this study, two main groups can be formed based on the noise performances. Group A ( $S3$ ,  $S3^{+}$  and  $S3^{\Delta}$ ) is characterized by a solid sawtooth serration and every member within this group consistently demonstrated a significant trailing edge broadband noise reduction. Group B ( $S3^{-}$  and  $S3^{\circ}$ ), where every member within this group utilizes sawtooth made from porous nickel-chromium foams, offers no advantage on the broadband noise reduction even though it shares the same geometrical parameters of serration as Group A. This might imply different acoustical scattering efficiency when the turbulent wavenumber components propagate on a porous sawtooth serration.

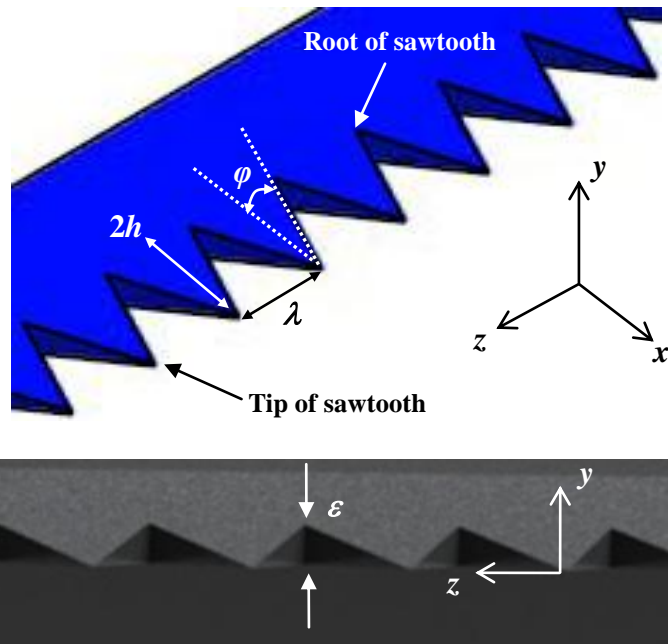
In conclusion, the poro-serrated trailing edges investigated in this paper have the potential to improve the industrial worthiness of the serration technology in achieving low noise radiation in fan and turbine blades. A viable path for the continuation of the current work is a parametric study when the poro-serrated trailing edge is subjected to different sawtooth geometries (e.g.  $2h$  and  $\varphi$ ) and porous materials with different air flow resistivity, density, permeability and surface roughness, over a wide range of Reynolds numbers and angles of attack.

### **Acknowledgments**

The authors are grateful for the support from the EPSRC Doctoral Training Grants in the United Kingdom, and would like to thank Elisa Dubois and Chioma Muhammad for their help in acquiring some of the experimental data.


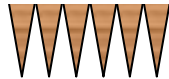
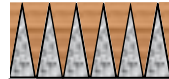


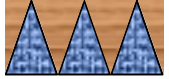




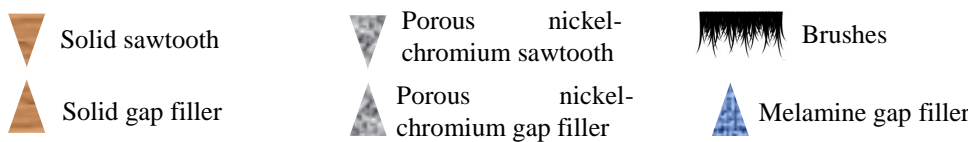
## References

- [1] Gruber, M., Joseph, P. F. and Chong, T. P., “Experimental Investigation of Airfoil Self Noise and Turbulent Wake Reduction by the use of Trailing Edge Serrations,” *16<sup>th</sup> AIAA/CEAS Aeroacoustic Conference and Exhibit*, AIAA Paper 2010–3803, 2010, Stockholm, Sweden.
- [2] Oerlemans, S., Fisher, M., Maeder, T. and Korler, K., “Reduction of Wind Turbine Noise using Optimized Airfoils and Trailing Edge Serrations,” *AIAA Journal*, Vol. 47, 2009, pp. 1470–1481.
- [3] Moreau, D. J. and Doolan C. J., “Noise-Reduction Mechanism of a Flat-Plate Serrated Trailing Edge,” *AIAA Journal*, Vol. 51, 2013, pp. 2513–2522.
- [4] Geyer, T., Sarradj, E. and Fritzsche, C., “Measurement on the Noise Generation at the Trailing Edge of Porous Airfoils,” *Experiment in Fluids*, Vol. 48, 2010, pp. 291–308.
- [5] Herr, M., “Design Criteria for Low-Noise Trailing-Edges,” *13<sup>th</sup> AIAA/CEAS Aeroacoustic Conference and Exhibit*, AIAA Paper 2007–3470, 2007, Rome, Italy.
- [6] Finez, A., Jondeau, E., Roger, M. and Jacob, M. C., “Broadband Noise Reduction with Trailing Edge Brushes,” *16<sup>th</sup> AIAA/CEAS Aeroacoustic Conference*, AIAA Paper 2010–3980, 2010, Stockholm, Sweden.
- [7] Chong, T. P., Vathylakis, A., Joseph, P. F. and Gruber, M., “Self-Noise Produced by an Airfoil with Nonflat plate Trailing-Edge Serrations,” *AIAA Journal*, Vol. 51, 2013, pp. 2665–2677.
- [8] Chong, T. P., Joseph, P. F. and Gruber, M., “Airfoil Self Noise Reduction by Non-Flat plate type Trailing Edge Serrations,” *Applied Acoustics*, Vol. 74, 2013, pp. 607–613.
- [9] Vathylakis, A., Chong, T. P. and Kim, J. H., “Design of a Low-Noise Aeroacoustic Wind Tunnel Facility at Brunel University,” *20<sup>th</sup> AIAA/CEAS Aeroacoustic Conference and Exhibit*, AIAA Paper 2014–3288, 2014, Atlanta, Georgia.
- [10] Chong, T. P., Joseph, P. F. and Davies, P. O. A. L., “Design and Performance of an Open Jet Wind Tunnel for Aero-Acoustic Measurement,” *Applied Acoustics*, Vol. 70, 2009, pp. 605–614.
- [11] Howe, M. S., “Noise produced by a Sawtooth Trailing Edge,” *Journal of the Acoustical Society of America*, Vol. 90, 1991, pp. 482–487.
- [12] Gruber, M., Joseph, P. F. and Chong, T. P., “On the Mechanism of Serrated Airfoil Trailing Edge Noise Reduction,” *17<sup>th</sup> AIAA/CEAS Aeroacoustic Conference and Exhibit*, AIAA Paper 2011–2781, 2011, Portland, Oregon.
- [13] Geyer, T. and Sarradj, E., “Trailing Edge Noise of Partially Porous Airfoils,” *20<sup>th</sup> AIAA/CEAS Aeroacoustic Conference and Exhibit*, AIAA Paper 2014–3039, 2014, Atlanta, Georgia.
- [14] Chong, T. P. and Vathylakis, A., “On the Aeroacoustic and Flow Structures Developed on a Flat Plate with a Serrated Sawtooth Trailing Edge,” *Journal of Sound and Vibration*, Vol. 354, 2015, pp. 65–90.

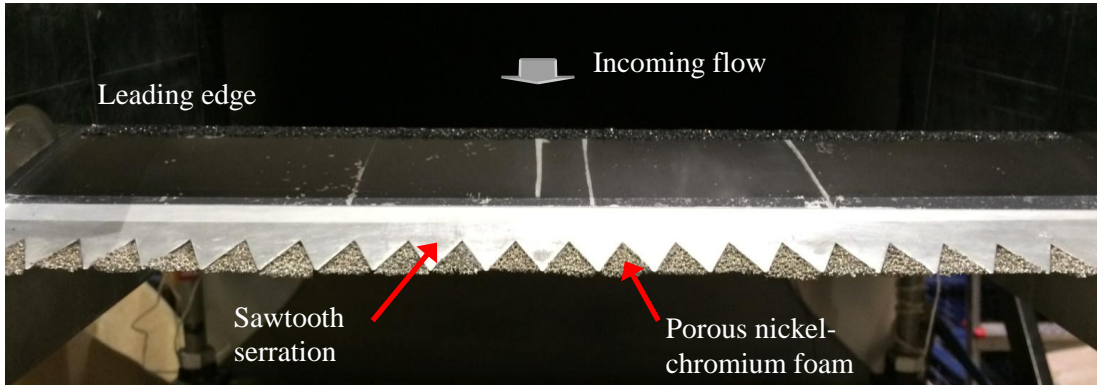


**Fig. 1** Parameters associated with a nonflat plate type sawtooth geometry: serration angle  $\phi$ , serration length  $2h$ , serration period  $\lambda$  and root bluntness  $\epsilon$ .

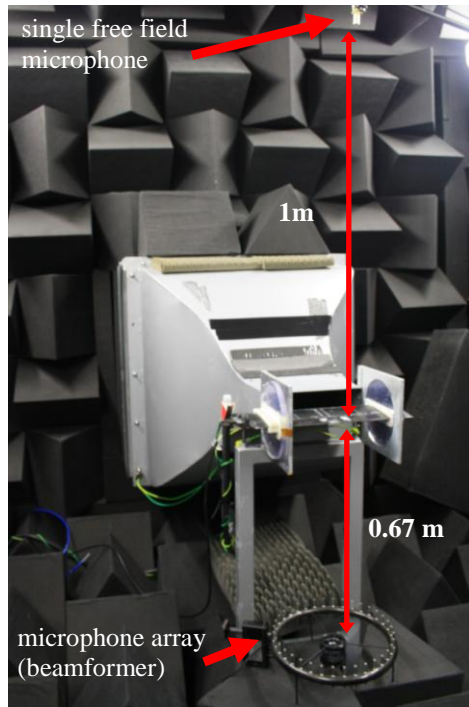


Symbols	Descriptions	Drawings
S0	Baseline, straight, nonporous solid trailing edge	
S1	Nonflat plate serrated trailing edge; $2h = 20$ mm, $\varphi = 7^\circ$ , $\lambda/h = 0.49$ and $\varepsilon = 5.7$ mm	
S1 <sup>+</sup>	<b>(Poro-Serrated trailing edge)</b> Same serration parameters as S1; sawtooth gaps filled with porous nickel-chromium foams	
S3	Nonflat plate serrated trailing edge; $2h = 20$ mm, $\varphi = 25^\circ$ , $\lambda/h = 1.87$ and $\varepsilon = 5.7$ mm	
S3 <sup>+</sup>	<b>(Poro-Serrated trailing edge)</b> Same serration parameters as S3; sawtooth gaps filled with porous nickel-chromium foams	
S3 <sup>++</sup>	<b>(Poro-Serrated trailing edge)</b> Same serration parameters as S3; sawtooth gaps filled with Melamine foams	
S3 <sup>-</sup>	“Inversed” poro-serrated trailing edge Same serration parameters as S3; sawtooth – porous nickel-chromium foam, sawtooth gaps – filled with nonporous, solid surface	
S3 <sup>Δ</sup>	<b>(Poro-Serrated trailing edge)</b> Same serration parameters as S3; sawtooth gaps <u>partially</u> filled with thin layer of brushes	
S3 <sup>o</sup>	Same serration parameters as S3; Sawtooth gaps (interstices) remain open; Sawtooth made from porous nickel-chromium foams	
SP	Partially porous, straight trailing edge; same porous nickel-chromium foams as in S1 <sup>+</sup> and S3 <sup>+</sup> ; $s = 2h$ of S1, S1 <sup>+</sup> , S3, S3 <sup>+</sup> , S3 <sup>++</sup> , S3 <sup>-</sup> , S3 <sup>Δ</sup> and S3 <sup>o</sup>	
		

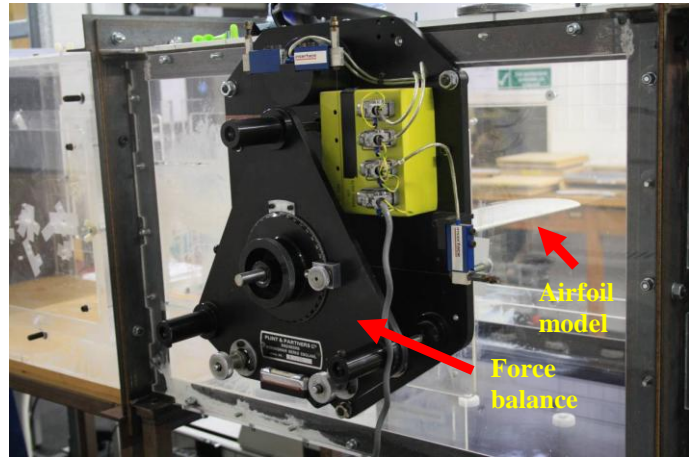
**Table 1** Summary of all trailing edge devices tested in this study. Trailing edge drawings are all subjected to mainstream flow from top to bottom. Drawings are not to scale.



**Fig. 2** Photograph of the S3<sup>+</sup> poro-serrated trailing edge installed on a NACA0012 airfoil.

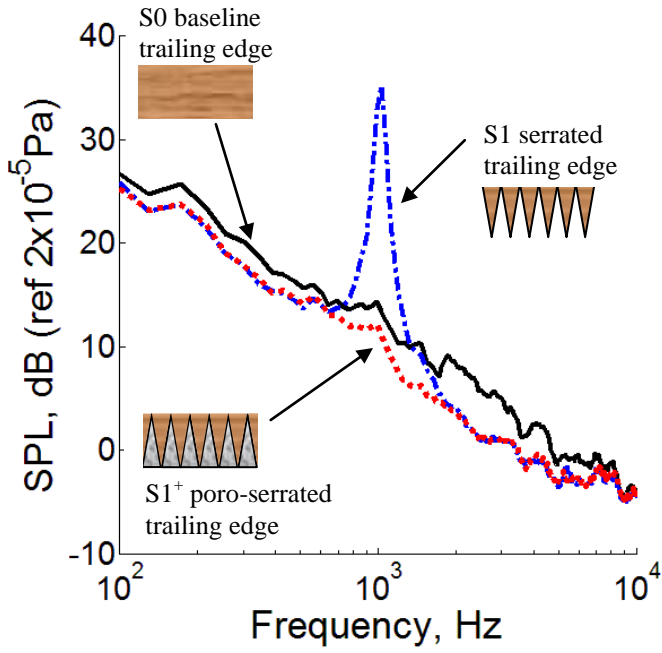


a)

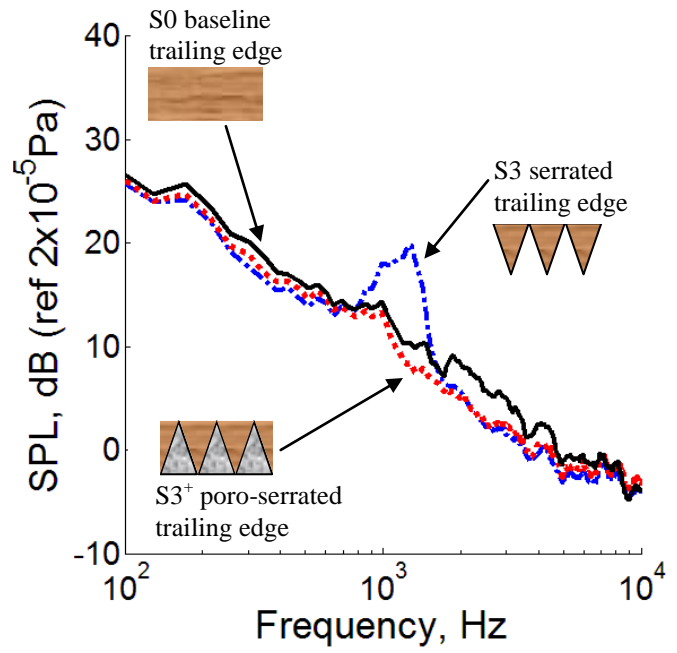


b)

**Fig. 3** Experiment setup for a) airfoil noise tests in the aeroacoustic wind tunnel facility and b) force balance used for lift and drag measurements in the aerodynamic wind tunnel.

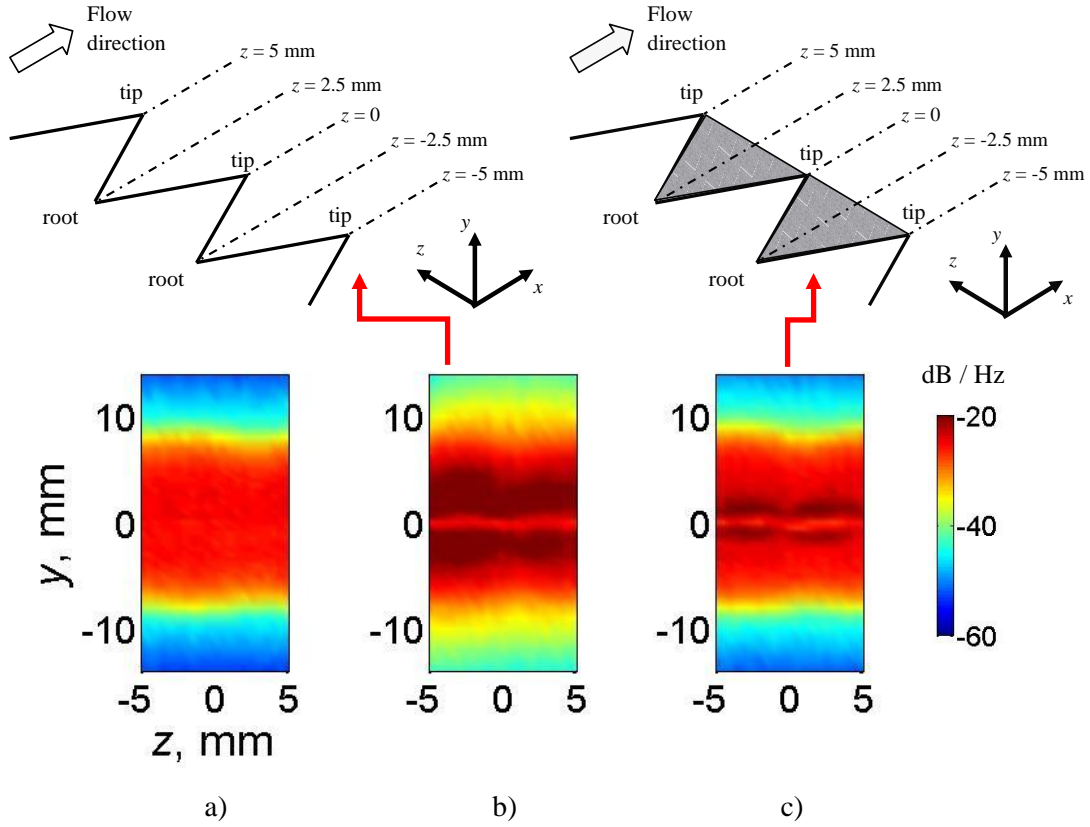


a)

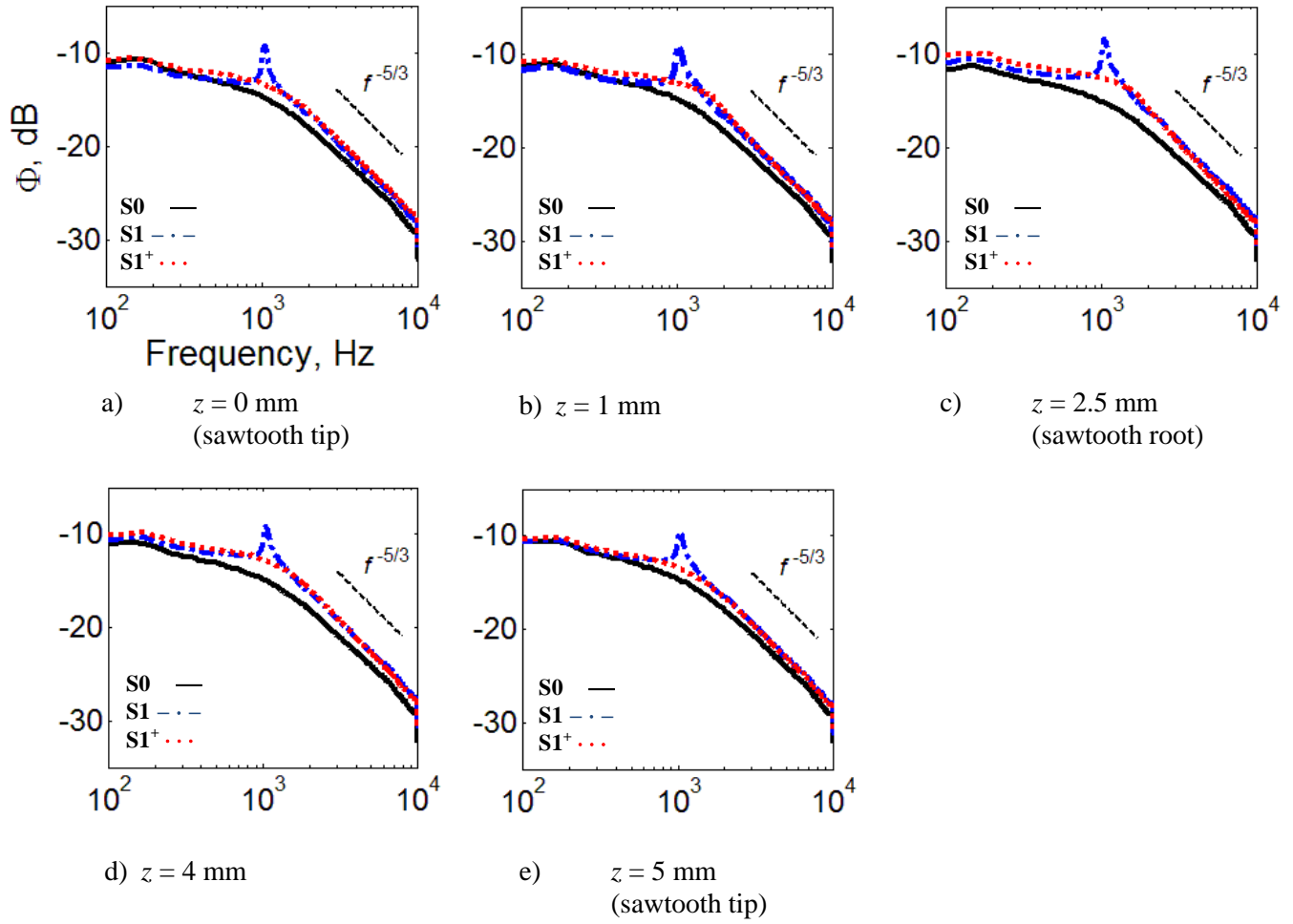


b)

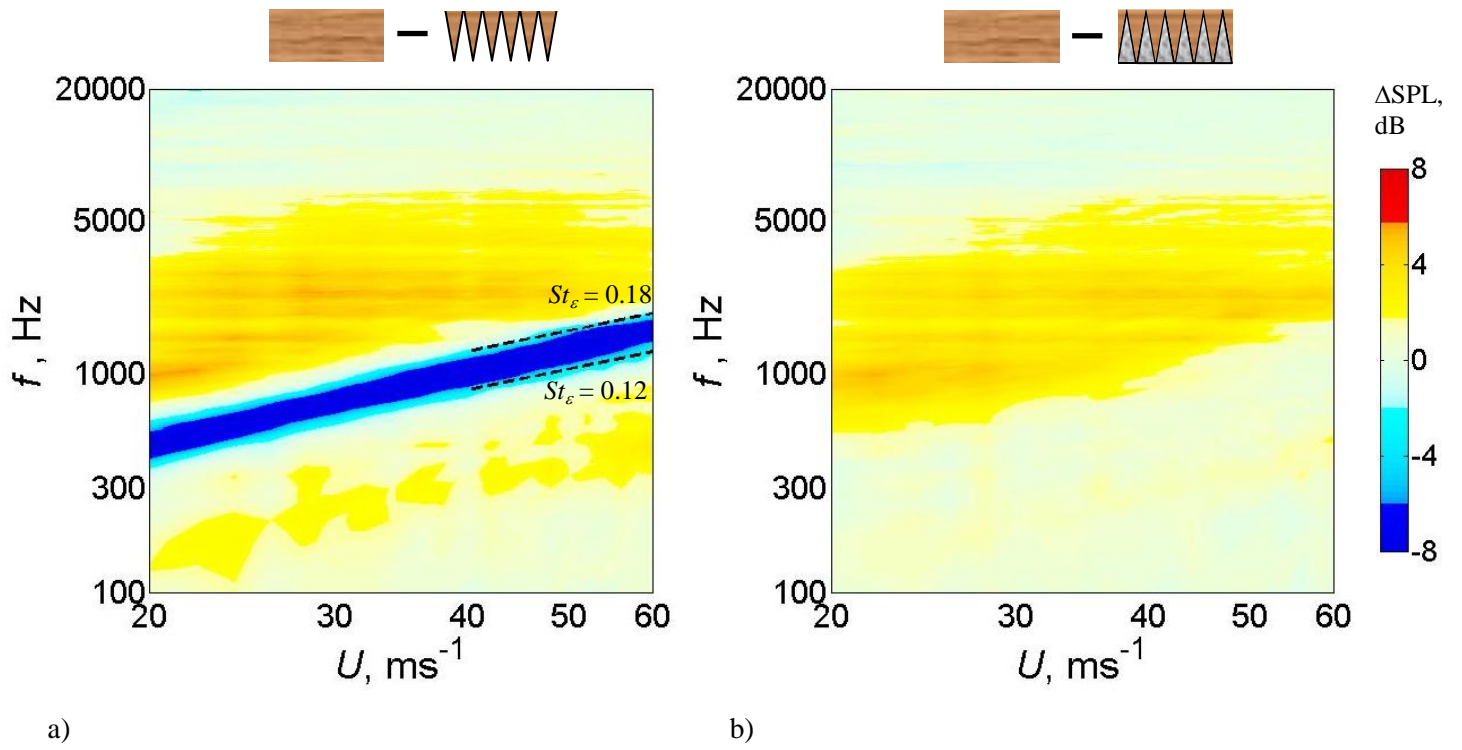
**Fig. 4** Comparisons of SPL, dB measured at  $U = 40 \text{ ms}^{-1}$  for a) S0, S1 and S1<sup>+</sup> trailing edges, and b) S0, S3 and S3<sup>+</sup> trailing edges.



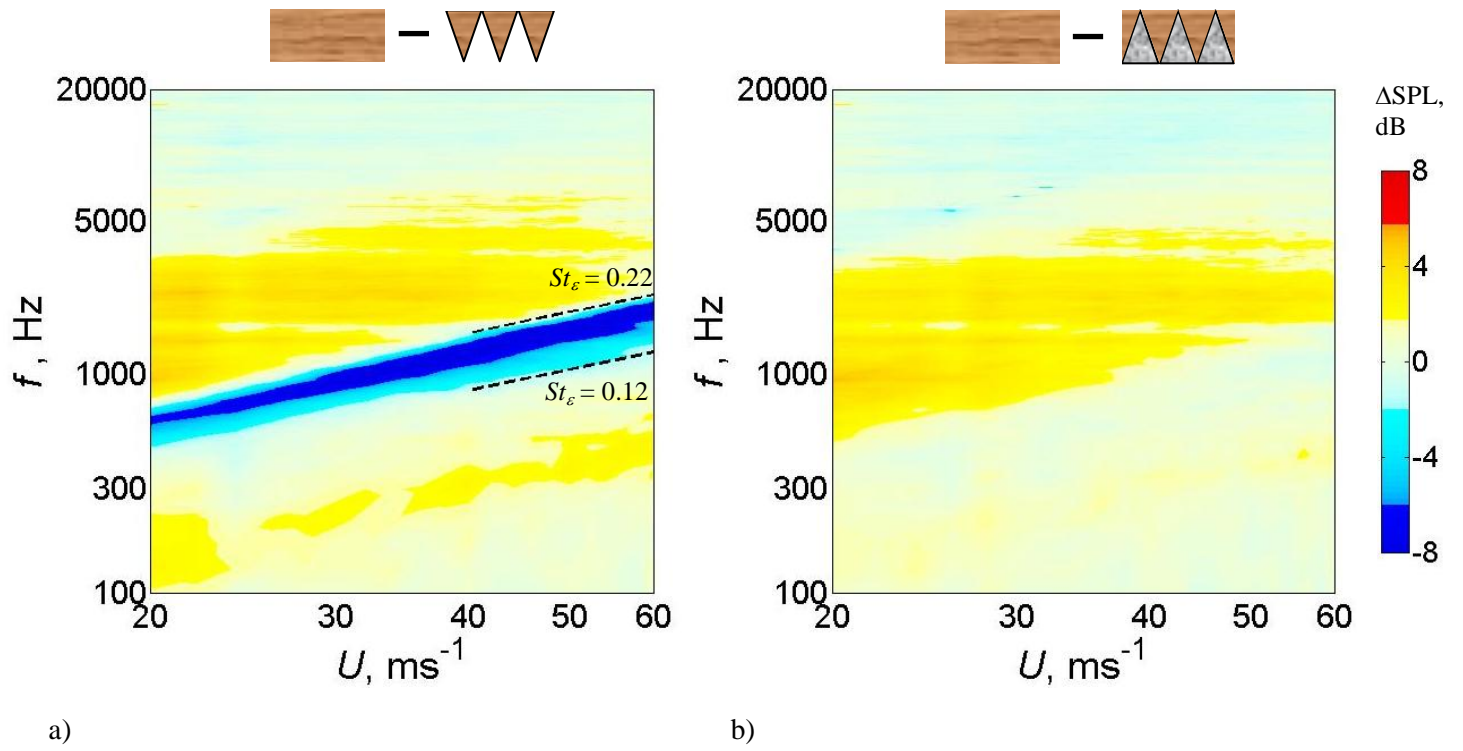
**Fig. 5** Comparisons of the near wake fluctuating velocity power spectral density (PSD) measured at  $x/C = 1.03$  and  $U = 40 \text{ ms}^{-1}$  for a) S0, b) S1, and c) S1<sup>+</sup> trailing edges. All PSD maps correspond to  $f = 1 \text{ kHz}$ .



**Fig. 6** Comparisons of near wake  $\Phi$ , dB measured at  $x/C = 1.03$  and  $U = 40 \text{ ms}^{-1}$  for S0, S1, and S1<sup>+</sup> trailing edges at various  $z$  locations.

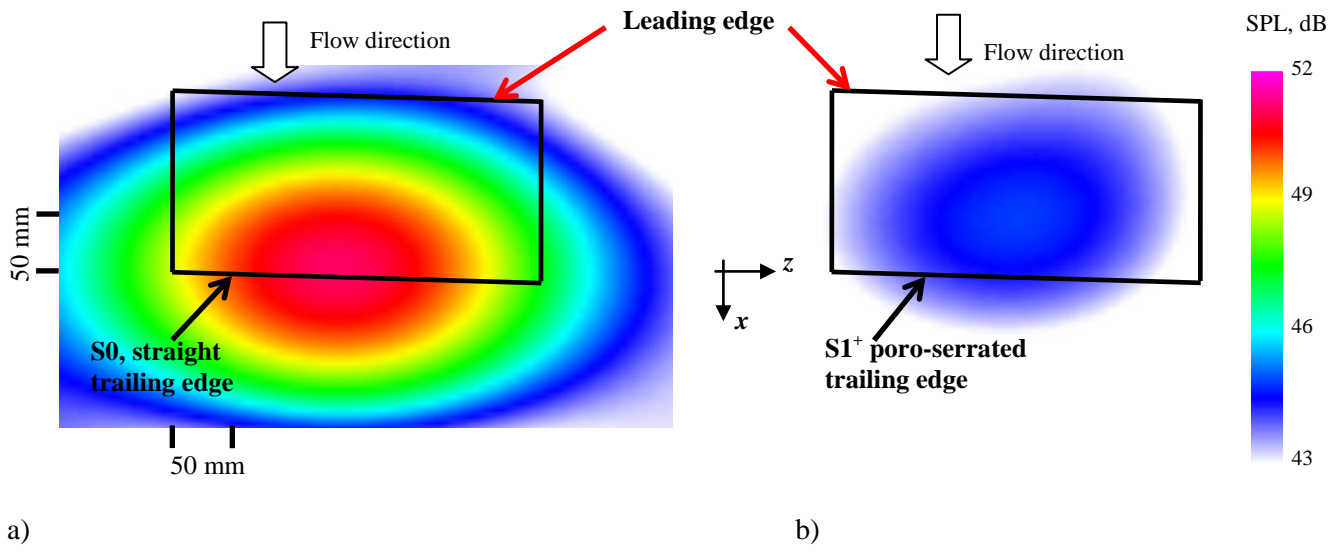


**Fig. 7** Color maps of the  $\Delta\text{SPL}$ , dB produced by a) S1 serrated trailing edge and b) S1<sup>+</sup> poro-serrated trailing edge. The velocity resolution is 2  $\text{ms}^{-1}$ .

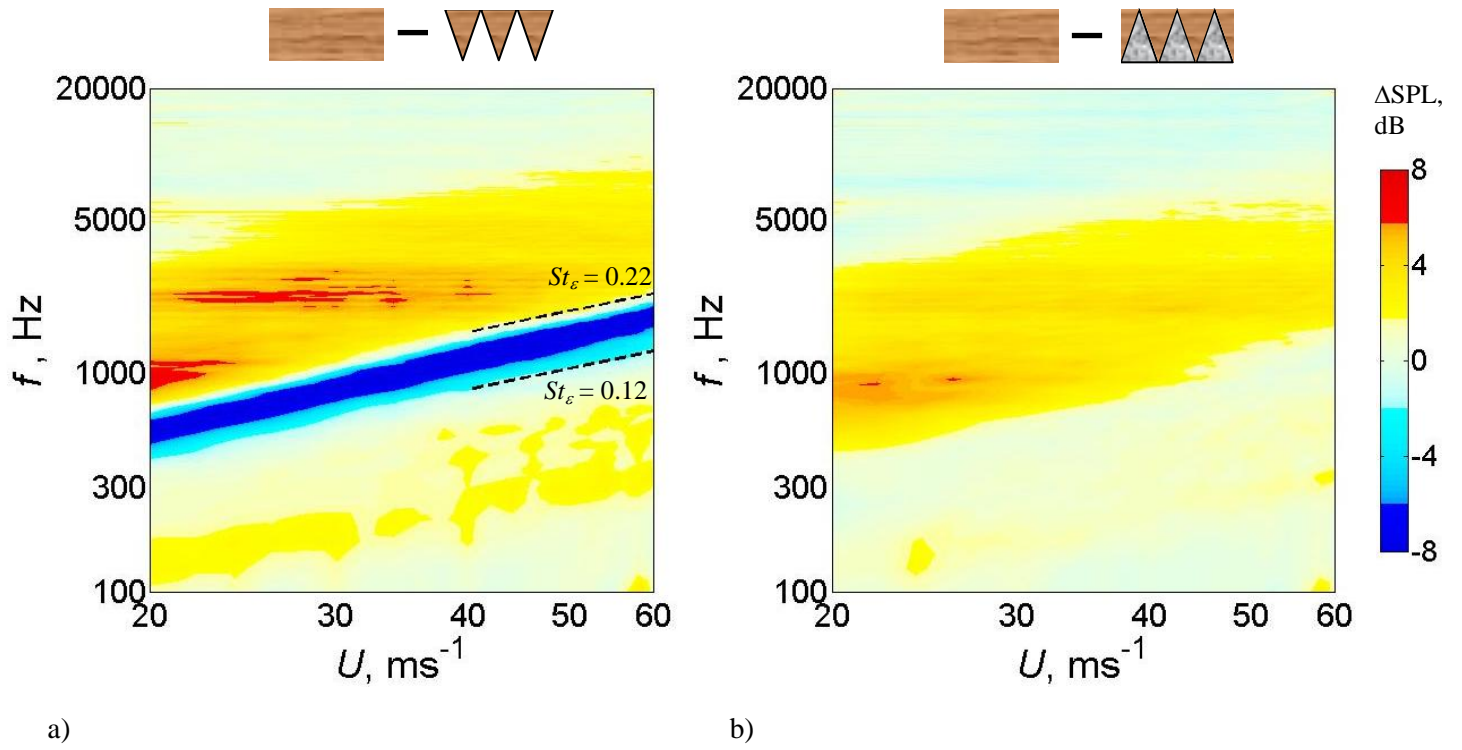


**Fig. 8** Color maps of the  $\Delta\text{SPL}$ , dB produced by a) S3 serrated trailing edge and b) S3<sup>+</sup> poro-serrated trailing edge. The velocity resolution is 2  $\text{ms}^{-1}$ .

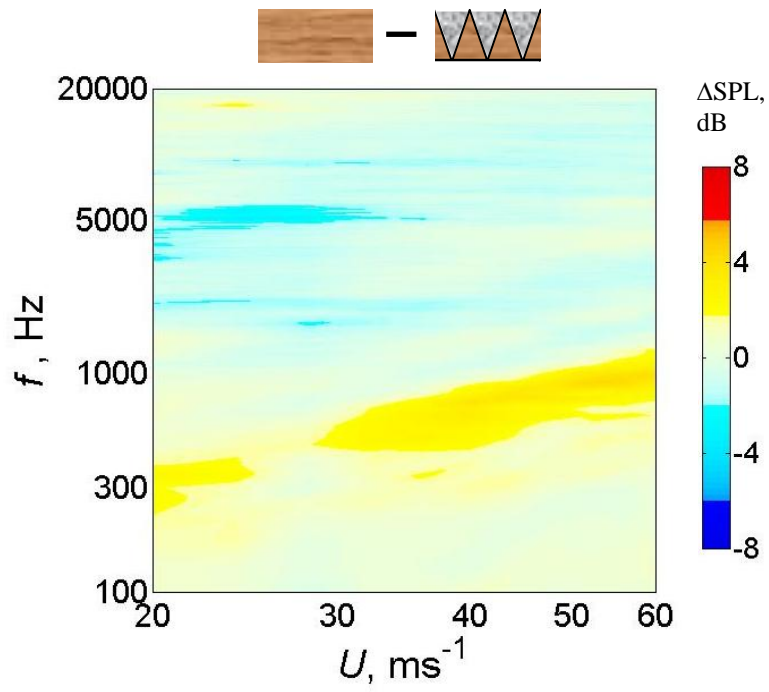




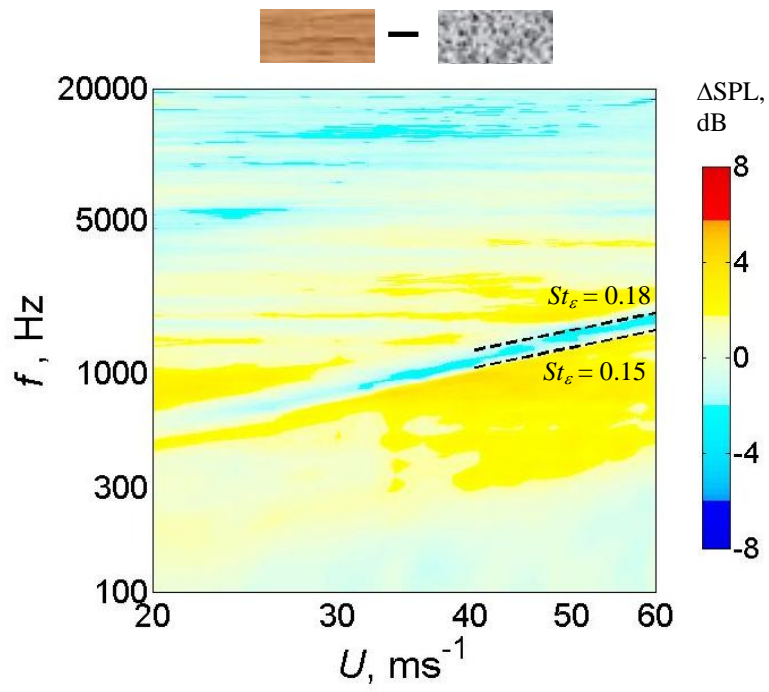
**Fig. 9** Comparisons of the beamformer maps at  $f = 2.3$  kHz at  $U = 40$  ms<sup>-1</sup> for a) baseline S0 straight trailing edge and b) S1<sup>+</sup> poro-serrated trailing edge.



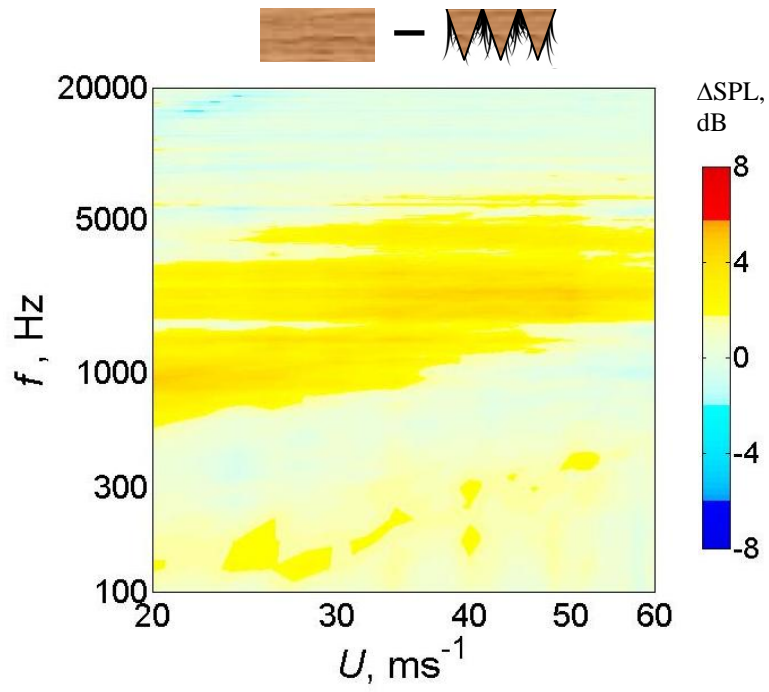
**Fig. 10** Color maps of the  $\Delta\text{SPL}$ , dB produced by a) S3 serrated trailing edge and b) S3<sup>+</sup> poro-serrated trailing edge. This repeatability test was performed at the ISVR anechoic chamber. The velocity resolution is  $2 \text{ ms}^{-1}$ .



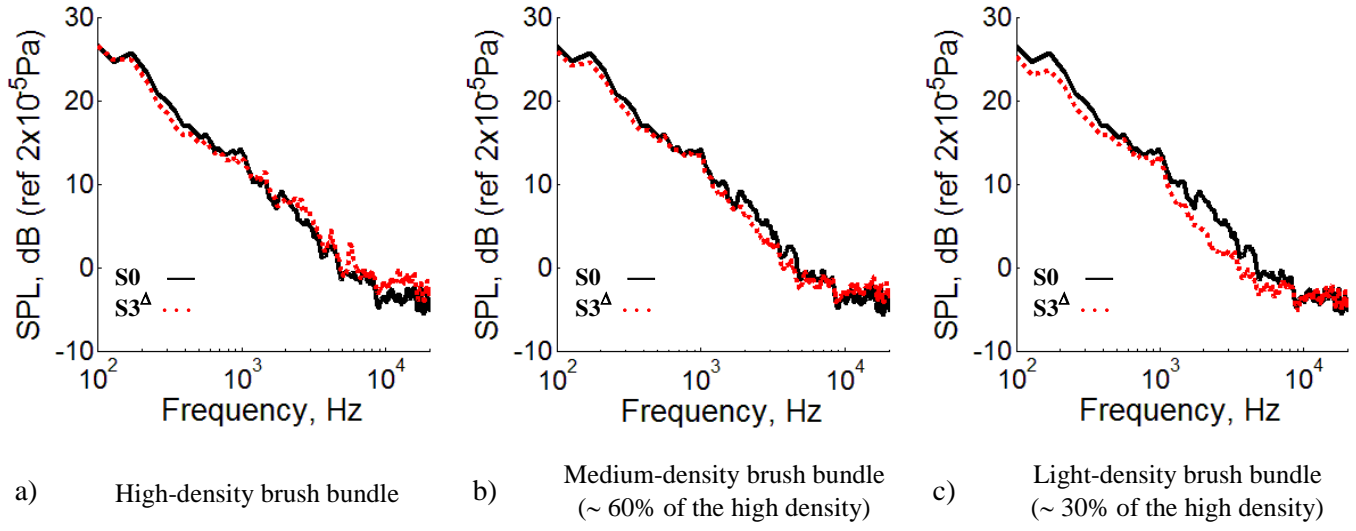
**Fig. 11** Color map of the  $\Delta\text{SPL}$ , dB produced by the S3<sup>-</sup> “inversed” poro-serrated trailing edge. The velocity resolution is 2  $\text{ms}^{-1}$ .



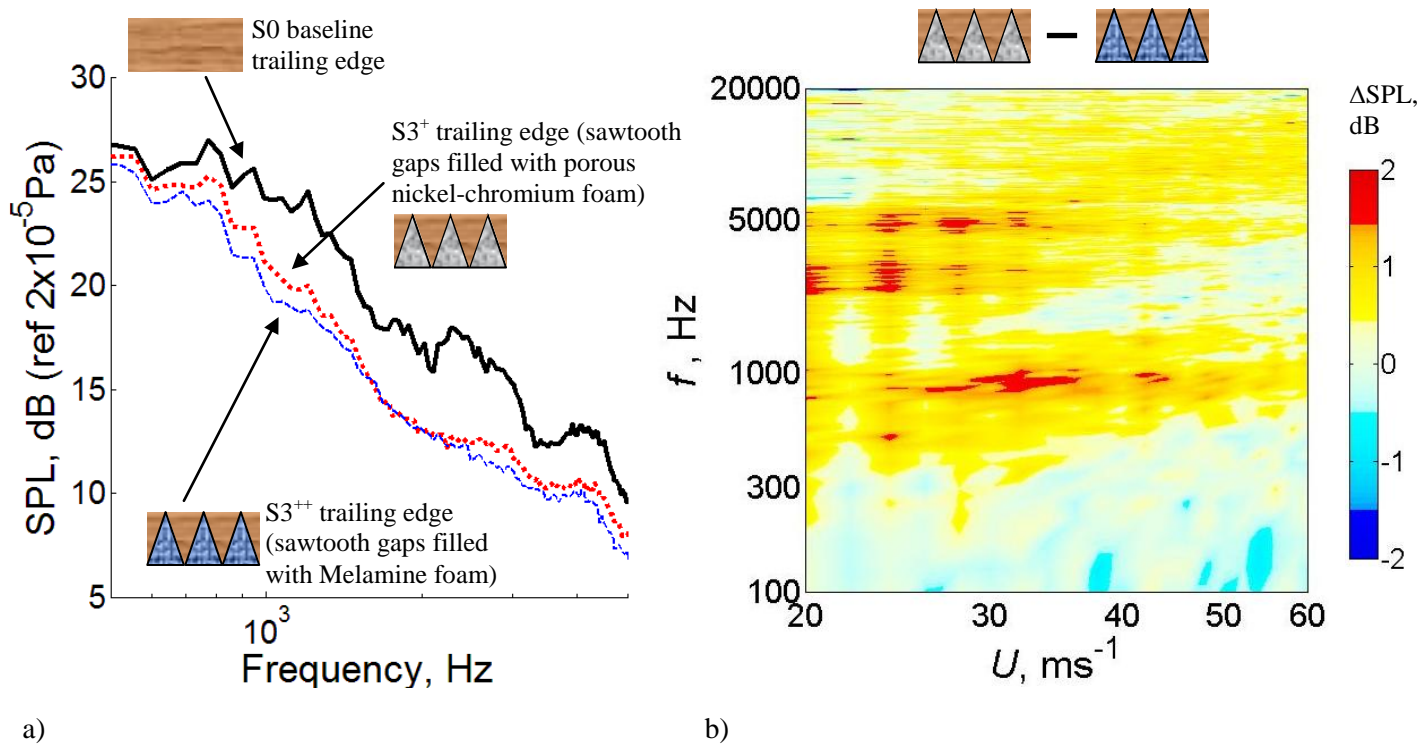
**Fig. 12** Color map of the  $\Delta\text{SPL}$ , dB produced by the SP partially porous trailing edge. The velocity resolution is  $2 \text{ ms}^{-1}$ .



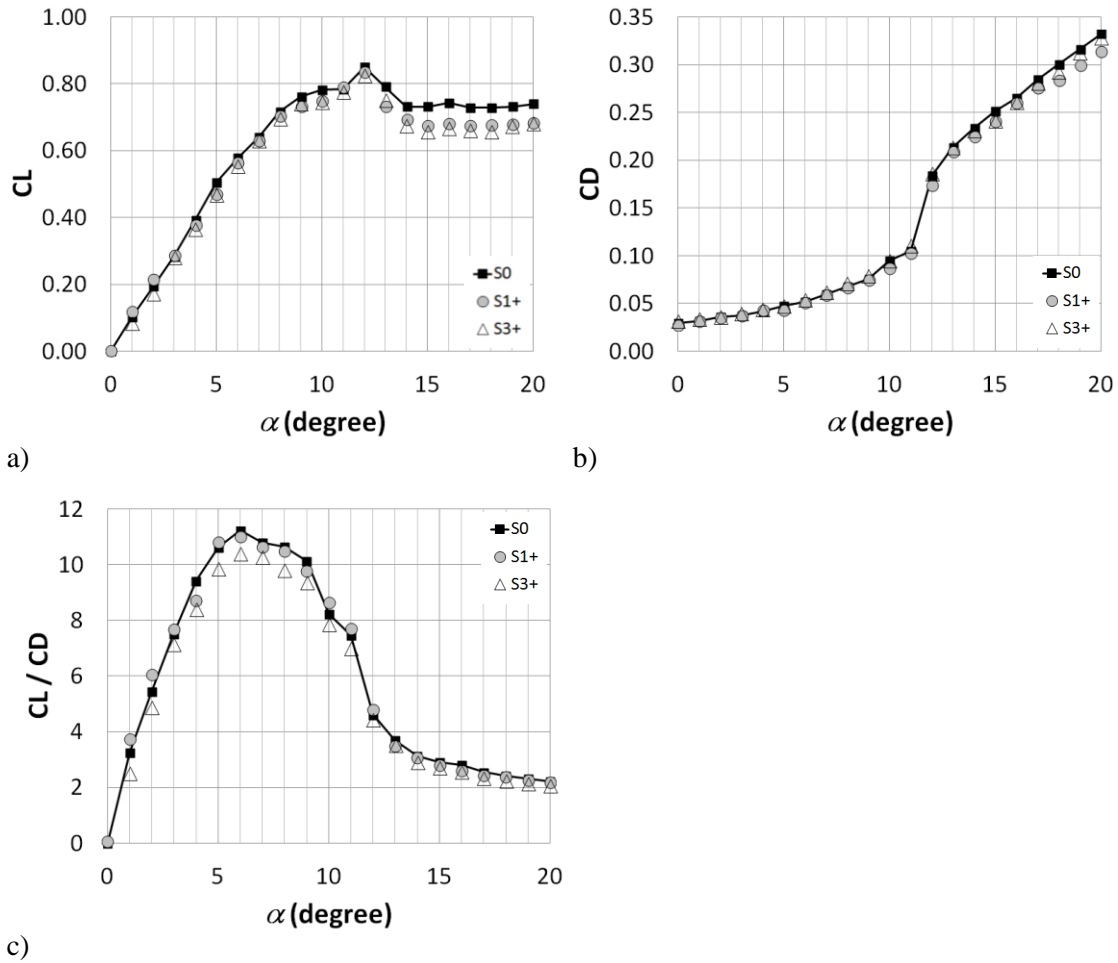
**Fig. 13** Color map of the  $\Delta\text{SPL}$ , dB produced by the S3<sup>A</sup> poro-serrated trailing edge. The velocity resolution is 2  $\text{ms}^{-1}$ .



**Fig. 14** Comparisons of the SPL, dB measured at  $U = 40 \text{ ms}^{-1}$  between the baseline S0 trailing edge and the S3<sup>A</sup> poro-serrated trailing edge with a) high-, b) medium-, and c) light-density brush bundles that fill the gaps between adjacent members of the sawtooth.

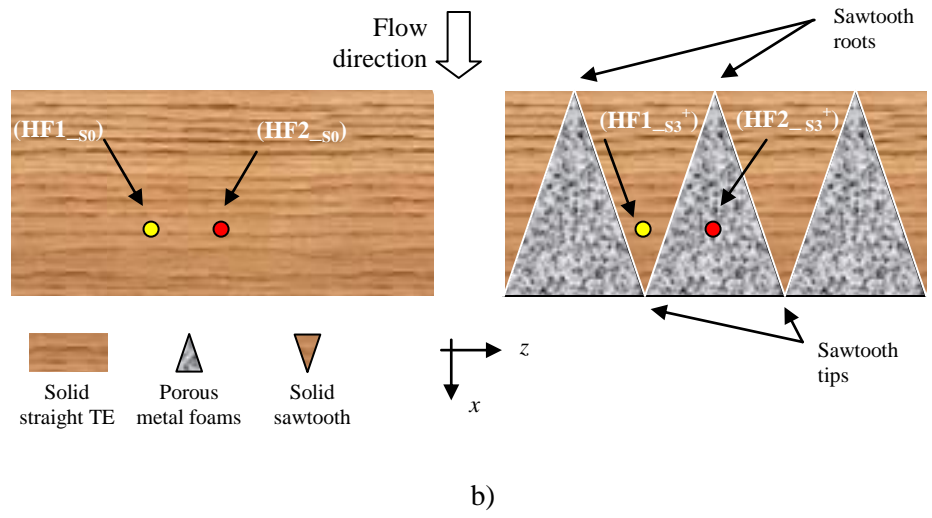


**Fig. 15** a) Comparisons between the S3<sup>+</sup> and S3<sup>++</sup> poro-serrated trailing edges in a) SPL, dB at  $U = 36 \text{ ms}^{-1}$  and b) Color map of  $\Delta$ SPL (S3<sup>+</sup> - S3<sup>++</sup>), dB at different frequency and velocity. The velocity resolution is  $2 \text{ ms}^{-1}$ .

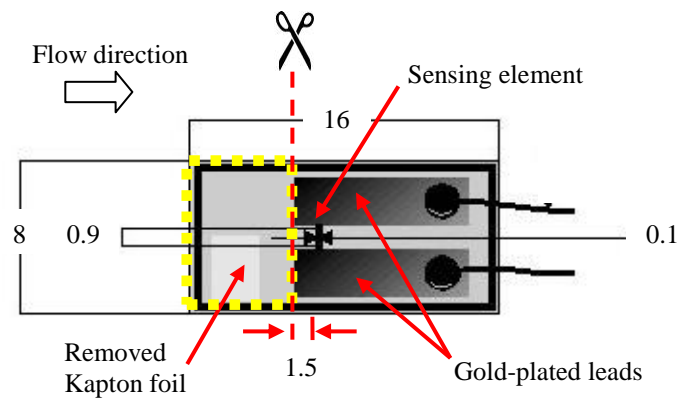


**Fig. 16** Comparisons of a) CL, b) CD and c) CL/CD against  $\alpha$  produced by S0 trailing edge (baseline) and S1<sup>+</sup> and S3<sup>+</sup> poro-serrated trailing edges at  $U = 30 \text{ ms}^{-1}$

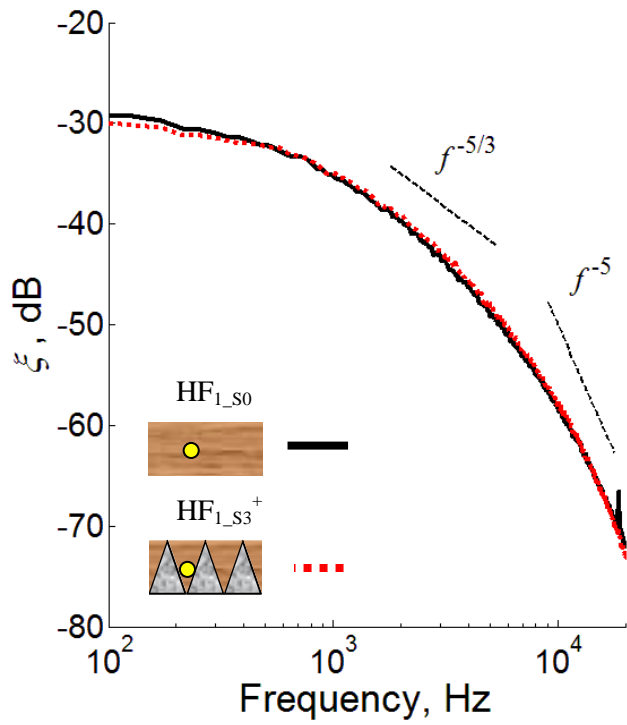




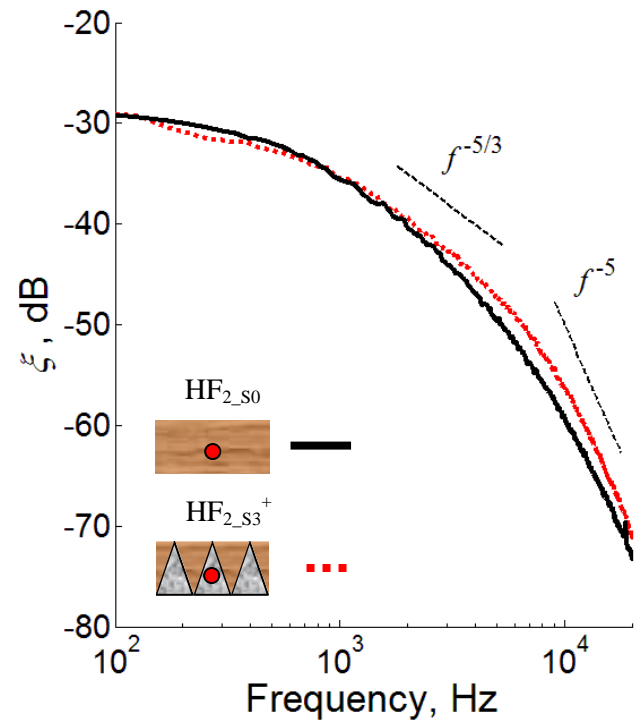
**Fig. 17** Schematics of locations of hot-film sensors HF1 and HF2 relative to a) S0 trailing edge and b) S3<sup>+</sup> poro-serrated trailing edge. Drawings are not to scale.



**Fig. 18** Schematics showing a surface-mounted hot-film sensor (Dantec, type 55R47) used in the current work. All units are in millimeters.

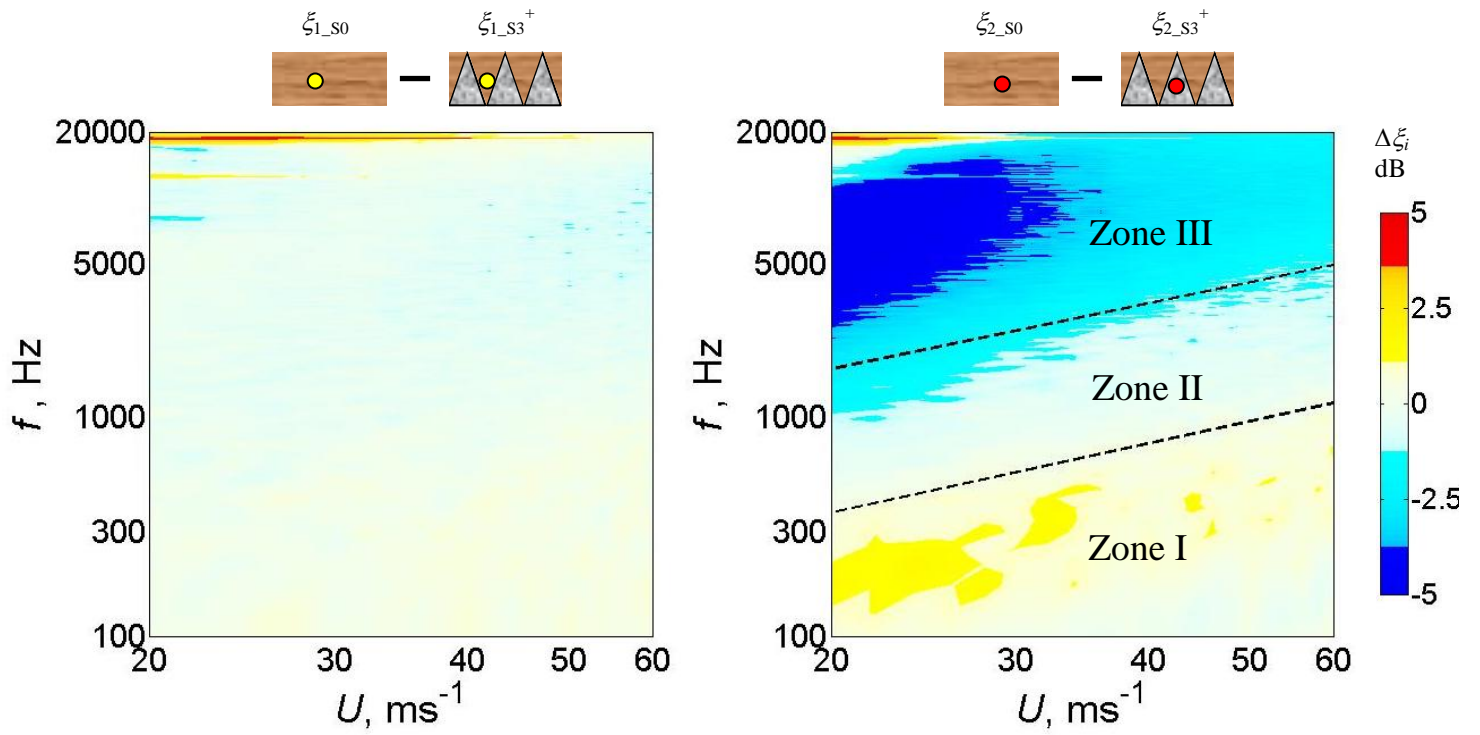


a)



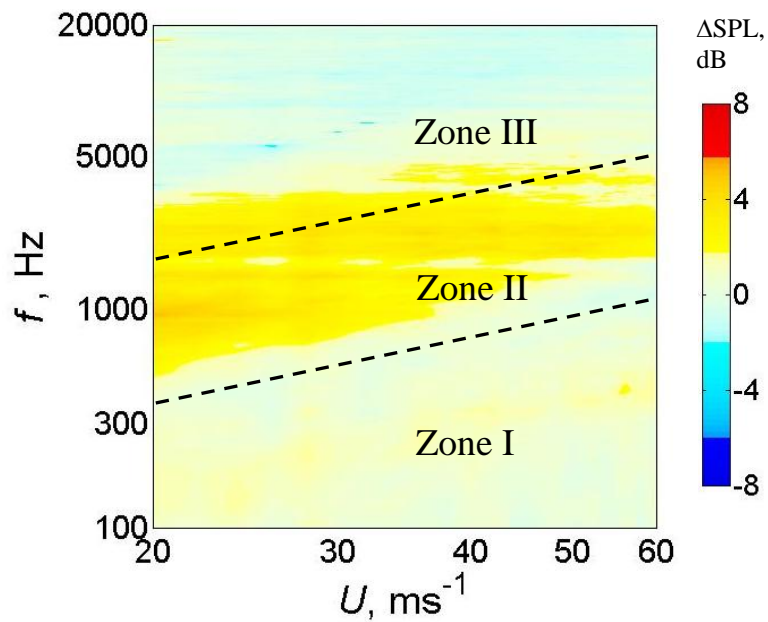
b)

**Fig. 19** Comparisons of the near wall fluctuating power spectral densities ( $\xi$ , dB) measured by hot-film sensors at  $U = 40 \text{ ms}^{-1}$ .




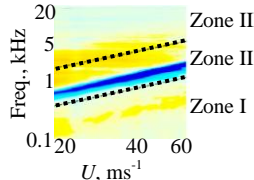

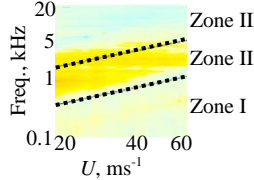

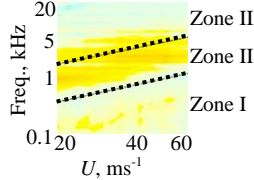
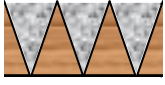
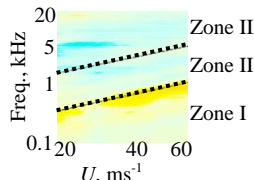

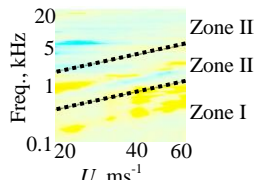

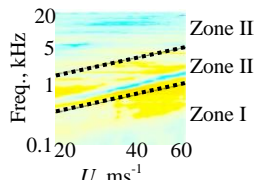
a)

b)



c)

**Fig. 20** Color maps of a)  $\Delta\xi_1$  and b)  $\Delta\xi_2$  [both calculated by Eq. (3)], and c)  $\Delta\text{SPL}$  produced by  $S3^+$  poro-serrated trailing edge [calculated by Eq. (2)].

Symbols	Illustrations		$\Delta\text{SPL}(f, U)^{a,b}$ , dB
S3		<b>Group A</b>	
S3 <sup>+</sup>			
S3 <sup>Δ</sup>			
S3 <sup>-</sup>		<b>Group B</b>	
S3 <sup>o</sup>			
SP			

a. Positive level of  $\Delta\text{SPL}$  denotes noise reduction, and vice versa.

b. The three zones (I, II and III) in the  $\Delta\text{SPL}$  maps were identified from the  $\Delta\xi_2$  contours in Fig. 20b.

**Table 2** Summary of all noise performances in  $\Delta\text{SPL}$ , dB, for S3, S3<sup>+</sup>, S3<sup>-</sup>, S3<sup>Δ</sup>, S3<sup>o</sup> and SP trailing edge devices investigated in this study.